



**HAL**  
open science

## Microtubules tune mechanosensitive cell responses

Shailaja Seetharaman, Benoit Vianay, Vanessa Roca, Aaron Farrugia, Chiara de Pascalis, Batiste Boëda, Florent Dingli, Damarys Loew, Stéphane Vassilopoulos, Alexander Bershadsky, et al.

► **To cite this version:**

Shailaja Seetharaman, Benoit Vianay, Vanessa Roca, Aaron Farrugia, Chiara de Pascalis, et al.. Microtubules tune mechanosensitive cell responses. *Nature Materials*, 2021, 10.1038/s41563-021-01108-x . pasteur-03096554v2

**HAL Id: pasteur-03096554**

**<https://pasteur.hal.science/pasteur-03096554v2>**

Submitted on 15 Nov 2021

**HAL** is a multi-disciplinary open access archive for the deposit and dissemination of scientific research documents, whether they are published or not. The documents may come from teaching and research institutions in France or abroad, or from public or private research centers.

L'archive ouverte pluridisciplinaire **HAL**, est destinée au dépôt et à la diffusion de documents scientifiques de niveau recherche, publiés ou non, émanant des établissements d'enseignement et de recherche français ou étrangers, des laboratoires publics ou privés.



Distributed under a Creative Commons Attribution - NonCommercial 4.0 International License

1 **Microtubules tune mechanosensitive cell responses**

2

3 **Shailaja Seetharaman<sup>1,2</sup>, Benoit Vianay<sup>3</sup>, Vanessa Roca<sup>1</sup>, Aaron Farrugia<sup>4</sup>, Chiara De Pascalis<sup>1</sup>, Batiste**

4 **Boëda<sup>1</sup>, Florent Dingli<sup>5</sup>, Damarys Loew<sup>5</sup>, Stéphane Vassilopoulos<sup>6</sup>, Alexander Bershadsky<sup>4</sup>, Manuel**

5 **Théry<sup>3</sup>, Sandrine Etienne-Manneville<sup>1\*</sup>**

6

7 <sup>1</sup> Cell Polarity, Migration and Cancer Unit, Institut Pasteur, UMR3691 CNRS, Equipe Labellisée Ligue

8 Contre le Cancer, F-75015, Paris, France.

9 <sup>2</sup> Université Paris Descartes, Sorbonne Paris Cité, 12 Rue de l'École de Médecine, 75006 Paris, France.

10 <sup>3</sup> Paris University, INSERM, CEA, Hôpital Saint Louis, Institut Universitaire d'Hématologie, Paris, France.

11 <sup>4</sup> Mechanobiology Institute, National University of Singapore, T-lab, 5A Engineering Drive 1, Singapore,

12 117411, Singapore.

13 <sup>5</sup> Institut Curie, PSL Research University, Centre de Recherche, Laboratoire de Spectrométrie de Masse

14 Protéomique, 26 rue d'Ulm, Paris 75248 Cedex 05, France.

15 <sup>6</sup> Sorbonne Université, INSERM UMRS 974, Institute of Myology, Paris, France.

16

17 \*Correspondence: setienne@pasteur.fr

18

19

20

21

## 22 **Abstract**

---

23

24 Mechanotransduction is a process by which cells sense the mechanical properties of their surrounding  
25 environment, and adapt accordingly to perform cellular functions such as adhesion, migration and  
26 differentiation. Integrin-mediated focal adhesions are major sites of mechanotransduction, and their  
27 connection with the actomyosin network is crucial for mechanosensing as well as the generation and  
28 transmission of forces onto the substrate. Despite having emerged as major regulators of cell adhesion  
29 and migration, the contribution of microtubules to mechanotransduction still remains elusive. Here, we  
30 show that Talin- and actomyosin-dependent mechanosensing of substrate rigidity controls microtubule  
31 acetylation (a tubulin post-translational modification) by promoting the recruitment of alpha-tubulin  
32 acetyl transferase ( $\alpha$ TAT1) to focal adhesions. Microtubule acetylation tunes mechanosensitivity of focal  
33 adhesions and YAP translocation, and in turn, promotes GEF-H1-mediated RhoA activation, actomyosin  
34 contractility, and traction forces. Our results reveal a fundamental crosstalk between microtubules and  
35 actin in mechanotransduction that contributes to mechanosensitive cell adhesion and migration.

## 36 **Main**

---

37

38 Cells sense the physical properties of their environment, translate them into biochemical signals and  
39 adapt their behaviour accordingly. This process known as mechanotransduction is crucial during  
40 development and in the adult, during physiological and pathological conditions such as cell migration,  
41 wound healing and cancer<sup>1,2</sup>. Integrin-mediated focal adhesions (FAs) sense the matrix rigidity, control  
42 the generation of actomyosin-dependent forces and the transmission of these traction forces onto the  
43 substrate as well as contribute to mechanosensitive cell responses such as migration<sup>3,4</sup>. In addition to  
44 the actin cytoskeleton, microtubules are also key regulators of 2D and 3D cell migration<sup>5-8</sup>. Several  
45 studies have demonstrated the role of the actomyosin cytoskeleton and FAs in mechanotransduction;

46 however, very little is known about microtubules in this context. In this study, we used primary rat  
47 astrocytes and primary human umbilical vein endothelial cells (HUVECs) (both types of cells are  
48 dependent on efficient microtubule dynamics for migration or invasion<sup>9-13</sup>), to address the role of  
49 microtubules in rigidity sensing and mechanosensitive migration.

50 The crucial factors affecting the functions of the microtubule network are post-translational  
51 modifications (PTMs) of tubulin such as acetylation, which occurs at the K40 residue of  $\alpha$ -tubulin. The  
52 enzyme responsible for microtubule acetylation,  $\alpha$ TAT1 ( $\alpha$ -tubulin acetyltransferase 1, also called as  
53 MEC-17), is present in the lumen of microtubules<sup>14</sup> and is highly specific to  $\alpha$ -tubulin K40. On the other  
54 hand, the enzymes involved in deacetylation at K40 are histone deacetylase family member 6 (HDAC6)  
55 and sirtuin type 2 (Sirt2), both of which target other substrates as well<sup>15</sup>. In this study, we used  
56 previously characterized siRNAs targeting  $\alpha$ TAT1<sup>13</sup> (set 1: si $\alpha$ TAT1-1 and set 2: si $\alpha$ TAT1-2; [Extended Data](#)  
57 [Fig. 1a, 1b and 1c](#)) to decrease acetylation, and Tubacin ([Extended Data Fig. 1a and 1c](#)), a drug which  
58 increases microtubule acetylation by inhibiting HDAC6 without modifying the acetylation of other  
59 HDAC6 substrates such as histones<sup>16,17</sup>.

60

## 61 **Substrate rigidity promotes microtubule acetylation through integrin $\beta_1$** 62 **signalling**

---

63

64 We have previously shown that microtubules come in close proximity to FAs, and that microtubule  
65 acetylation promotes FA turnover during migration<sup>13</sup>. Since FAs are major mechanosensitive  
66 structures<sup>18</sup>, we investigated whether the extracellular matrix rigidity affects microtubule acetylation.  
67 Astrocytes were plated sparsely on polyacrylamide hydrogels of different rigidities: 1.26 kPa, 2 kPa, 9  
68 kPa and 48 kPa ([Fig. 1a and 1b](#)). Astrocytes on soft substrates exhibited lower levels of acetylated  
69 tubulin than cells on stiff substrates ([Fig. 1a and 1b](#)). Tubulin acetylation levels showed a two fold  
70 increase with increasing rigidity (1.26 kPa to 48 kPa), a strongly significant change in comparison to the

71 maximal 3.8 fold increase obtained after Tubacin treatment ([Extended Data Fig. 1d](#)). Subsequently, to  
72 determine whether microtubule acetylation may be indirectly caused by a mechanism involving  
73 differential cell spreading, we plated astrocytes on adhesive micropatterns (area 2500  $\mu\text{m}^2$ ) printed on 2  
74 kPa and 40 kPa hydrogels ([Extended Data Fig. 1e](#)). Similar to stiff substrates, astrocytes on soft  
75 substrates adopted a crossbow shape and identical spread area, and yet, microtubule acetylation was  
76 increased on stiff substrates as compared to softer substrates ([Extended Data Fig. 1e](#)). In contrast to  
77 tubulin acetylation, tubulin detyrosination (another tubulin PTM), remained unaffected by increased  
78 substrate rigidity in astrocytes ([Extended Data Fig. 1f and 1g](#)), and had no effect on astrocyte adhesion  
79 and migration<sup>13</sup>, suggesting that rigidity sensing specifically affects microtubule acetylation.

80

81 Integrin-based FAs sense the matrix rigidity and trigger mechanosensitive signalling pathways<sup>19</sup>. To  
82 determine the role of integrin signalling in controlling microtubule acetylation, we first used a scratch-  
83 induced migration assay to trigger integrin activation at the wound edge<sup>11</sup>. Addition of cyclic RGD (cRGD)  
84 peptide, to prevent the binding of integrins to the RGD motif of extracellular matrix proteins, reduced  
85 tubulin acetylation ([Extended Data Fig. 2a](#)). Furthermore, integrin activation using  $\text{MnCl}_2$ <sup>20</sup> led to an  
86 increase in microtubule acetylation as compared to control cells ([Extended Data Fig. 2b](#)). Finally,  
87 depletion of  $\beta_1$  integrin using a siRNA ([Extended Data Fig. 2c](#)) also resulted in a significant decrease in  
88 tubulin acetylation as compared to control cells ([Extended Data Fig. 2c and 2d](#)), suggesting that  $\beta_1$   
89 integrins are major players in the control of microtubule acetylation. We then investigated the  
90 involvement of two central players in integrin signalling; the proto-oncogene c-Src and the Focal  
91 Adhesion Kinase (FAK). In migrating astrocytes, inhibition of Src (using Src kinase inhibitor 1 – referred to  
92 as Src kin 1) and FAK (using PF-562271) drastically reduced the levels of acetylated tubulin ([Extended](#)  
93 [Data Fig. 2e](#)). In addition, following Src and FAK inhibition, microtubule acetylation induced by cell  
94 spreading on 48 kPa substrates was decreased to a level similar to that observed on soft substrates ([Fig.](#)

95 [1C and Extended Data Fig. 2f](#)), indicating that Src and FAK are required for the rigidity-dependent  
96 increase in acetylation. Altogether, these results strongly suggest that  $\beta_1$  integrin-mediated signalling  
97 promotes substrate rigidity-induced acetylation of microtubules.

98

## 99 **$\alpha$ TAT1 interacts with Talin in mechanosensitive manner**

100

101 Microtubule acetylation is mediated by  $\alpha$ TAT1; however, the recruitment and/or activation of  
102  $\alpha$ TAT1 remains unknown<sup>21</sup>. Therefore, we carried out a quantitative mass spectrometry screen to  
103 identify interacting partners of  $\alpha$ TAT1 using HEK293 cells. The mass spectrometry data (data available  
104 via ProteomeXchange with identifier PXD015871; check methods for details; [Extended Data Fig. 2g](#))  
105 revealed interesting potential interactors, amongst which the proteins enriched in the gene ontology for  
106 focal adhesions depicted in red in [Extended Data Fig. 2g](#). One of the significant interactors on the mass  
107 spectrometry screen was Talin ([Extended Data Fig. 2g](#)), a mechanosensitive partner of integrins<sup>19</sup>. We  
108 confirmed the interaction of  $\alpha$ TAT1 with Talin using pulldown experiments. GST- $\alpha$ TAT1, but not GST  
109 alone, associated with endogenous Talin from astrocyte lysates ([Fig. 1d and Extended Data Fig. 2h](#)). The  
110 interaction was further confirmed by immunoprecipitation using GFP- $\alpha$ TAT1-transfected astrocytes.  
111 Talin co-immunoprecipitated with GFP- $\alpha$ TAT1 but not with GFP alone ([Fig. 1e and Extended Data Fig. 2i](#)).  
112 In addition, using TIRF microscopy, we observed that GFP- $\alpha$ TAT1 strongly localised at mCherry-vinculin-  
113 positive FAs ([Fig. 1f](#))<sup>13</sup>. We then investigated whether Talin played a role in the recruitment of  $\alpha$ TAT1 to  
114 FAs and the acetylation of microtubules. Therefore, we used specific siRNAs to reduce Talin expression  
115 in primary astrocytes ([Extended Data Fig. 2j](#)). Talin depletion reduced GFP- $\alpha$ TAT1 recruitment to FAs  
116 ([Fig. 1f](#)). In addition, Talin-depleted astrocytes plated on 48 kPa substrates exhibited decreased levels of  
117 tubulin acetylation as compared to the control cells ([Fig. 1g](#)).

118

119 Since  $\alpha$ TAT1 is also present within microtubules (Extended Data Fig. 2k)<sup>13,14</sup>, we tested whether the  
120 recruitment of  $\alpha$ TAT1 to FAs was dependent on microtubules. To address this, GFP- $\alpha$ TAT1 and mCherry-  
121 vinculin expressing astrocytes were treated with Nocodazole to depolymerize all microtubules.  
122 Nocodazole-treated astrocytes displayed larger adhesions and increased stress fibres as observed in  
123 other cell types (Extended Data Fig. 2l, Supplementary Video 1)<sup>22,23</sup>, and increased  $\alpha$ TAT1 at FAs  
124 (Extended Data Fig. 2l, Supplementary Video 1), suggesting that microtubules are not required to  
125 localise  $\alpha$ TAT1 at FAs, and that increased actomyosin contractility might facilitate  $\alpha$ TAT1 concentration  
126 at FAs. Since actomyosin contractility is required for Talin-mediated mechanosensing<sup>24,25</sup>, we used the  
127 ROCK inhibitor, Y-27632 (which strongly reduces actomyosin contractility<sup>26</sup>) to assess its role in the  
128 mechanosensitive acetylation of microtubules. By GST- $\alpha$ TAT1 pulldown as well as TIRF microscopy, we  
129 observed that Y-27632 treatment decreased  $\alpha$ TAT1 interaction with Talin (Fig. 1h and 1i, Supplementary  
130 Video 2) and tubulin acetylation (Fig. 1j and 1k) confirming that actomyosin contractility and  
131 mechanosensing at FAs influence microtubule acetylation. Altogether, these results suggest that Talin-  
132 and actomyosin-dependent mechanosensing triggers the recruitment of  $\alpha$ TAT1 to FAs, and is required  
133 for rigidity-dependent microtubule acetylation.

134

## 135 **Microtubule acetylation influences mechanotransduction at focal adhesions**

---

136

137 We then tested whether microtubule acetylation may be involved in mechanosensitive cell  
138 functions. Astrocytes were sparsely plated on soft (2 kPa) and stiff (48 kPa) polyacrylamide hydrogels  
139 and stained for Yes-associated protein (YAP), an actomyosin- and RhoGTPase-dependent transcriptional  
140 activator whose nuclear translocation is mechanosensitive<sup>27</sup>. Like in several cell types<sup>28</sup>, quantification of  
141 nuclear-to-cytoplasmic ratio of YAP indicated that YAP nuclear localisation increased when astrocytes  
142 were plated on stiff substrates compared to soft substrates (Fig. 2a and 2b). In  $\alpha$ TAT1-depleted

143 astrocytes, the nuclear recruitment of YAP in cells plated on 48 kPa substrates was strongly inhibited  
144 and YAP localisation was similar in cells plated on soft and rigid substrates (Fig. 2a). Conversely,  
145 increasing microtubule acetylation by Tubacin treatment led to a strong nuclear recruitment of YAP in  
146 cells plated on 2 kPa substrates, recapitulating a phenotype of cells on stiff substrates (Fig. 2b). To  
147 determine whether the effects of microtubule acetylation on YAP were specific to astrocytes, we  
148 performed similar experiments on HUVECs. HUVECs exhibit low level of acetylated tubulin, even when  
149 plated on stiff substrates (Extended Data Fig. 3b, 3c). Hence, to test the effects of microtubule  
150 acetylation on YAP translocation in HUVECs, cells were treated with Tubacin to increase microtubule  
151 acetylation (Extended Data Fig. 3c). Similar to astrocytes, increasing microtubule acetylation in HUVECs  
152 plated on 2 kPa substrates resulted in an increased nuclear recruitment of YAP, mimicking the  
153 phenotype of cells plated on stiff substrates (Fig. 2c). Altogether, this demonstrates that the  
154 manipulation of microtubule acetylation tunes YAP mechanosensitive nuclear-cytoplasmic shuttling  
155 (summary cartoon shown in Fig. 2g).

156

157 FAs are crucial mechanosensitive structures which sense and adapt to the matrix rigidity<sup>29</sup>. Thus, we  
158 investigated the effects of substrate rigidity on FAs in astrocytes plated on polyacrylamide hydrogels of  
159 different rigidities: 1.26 kPa, 2 kPa, 9 kPa and 48 kPa (Fig. 2d), by immunostaining of the FA-associated  
160 protein, Paxillin<sup>4,30</sup>. Quantification of the density of FAs (Extended Data Fig. 3d) indicates that astrocytes  
161 plated on soft substrates display FAs throughout the cell surface, whereas, FAs are predominantly at the  
162 periphery of cells adhering to stiffer substrates (Fig. 2d). Thus, changes in substrate rigidity alter FA  
163 distribution in astrocytes, allowing us to assess the impact of microtubule acetylation in this  
164 phenomenon. Following  $\alpha$ TAT1 depletion, FAs were distributed throughout the cell surface  
165 independently of the rigidity of the substrate, i.e.,  $\alpha$ TAT1-depleted cells on stiff substrates showed a  
166 distribution of FAs similar as that of control/si $\alpha$ TAT1 cells plated on soft substrates (Fig. 2e, Extended



167 [Data Fig. 3e-3h](#)). To confirm that the changes in FA distribution act through tubulin acetylation, we  
168 treated cells plated on different rigidities with Tubacin. Tubacin had no effect on FA distribution in cells  
169 plated on 48 kPa substrates ([Fig. 2f, Extended Data Fig. 3e and 3f](#)). In contrast, Tubacin treatment of  
170 cells plated on 1.26 kPa substrates mimicked the phenotype (FAs at the cell periphery) observed in  
171 control/Tubacin-treated cells plated on stiff matrices ([Fig. 2f, Extended Data Fig. 3e and 3f](#)). Since cell  
172 spreading on different substrate rigidities can affect the distribution of FAs, we plated  $\alpha$ TAT1-depleted  
173 cells on micropatterned hydrogels to observe FAs in cells of similar spread area. In line with our prior  
174 results, cells on soft substrates or  $\alpha$ TAT1-depleted cells on stiffer substrates displayed FAs throughout  
175 the cell spreading area ([Extended Data Fig. 3i](#)). Together with previous findings that microtubule  
176 acetylation controls membrane vesicle delivery at FAs and FA dynamics<sup>13,31</sup>, these results show that the  
177 rigidity-dependent microtubule acetylation controls the mechanosensitive distribution of FAs ([Fig. 2g](#)).

178

## 179 **Microtubule acetylation controls cytoskeletal organization at focal adhesions**

---

180

181 Next, we investigated the impact of  $\alpha$ TAT1 depletion on the FA-associated cytoskeleton. In  
182 migrating astrocytes, the actin network comprises of longitudinal stress fibres connected to FAs at the  
183 front of the leader cells as well as inter-junctional transverse arcs connecting neighbouring cells at  
184 adherens junctions ([Fig. 3a and Extended Data Fig. 4a](#))<sup>26,32</sup>. In  $\alpha$ TAT1-depleted cells, the transverse arcs  
185 of actin were dramatically reduced and the longitudinal fibres did not extend to the front of migrating  
186 cells ([Fig. 3a, Extended Data Fig. 4a](#)). Associated with these longitudinal fibres, FAs were located further  
187 back within the protrusion rather than at the front of leader cells ([Fig. 3a and Extended Data Fig. 4a](#))<sup>13</sup>.  
188 Myosin light chain phosphorylation (pMLC) is predominantly seen at the leading edge of migrating  
189 control cells; however, in  $\alpha$ TAT1-depleted cells, pMLC was barely visible at the leading edge of cells and  
190 was only associated with the remaining actin fibres at the cell centre, similar to Myosin IIa distribution

191 (Fig. 3a, 3b and Extended Data Fig. 4a). Moreover, intermediate filaments (visualised using Vimentin),  
192 which play a major role in regulating FAs and collective migration of astrocytes<sup>32</sup> and normally extend  
193 from the perinuclear region to the cell periphery close to FAs<sup>32,33</sup>, were absent from the front of  $\alpha$ TAT1-  
194 depleted cells and frequently appeared fragmented (Fig. 3c). We then looked closely at the effect of  
195  $\alpha$ TAT1 on the cytoskeletal organisation at FAs by using platinum-replica transmission electron  
196 microscopy (EM) on unroofed migrating astrocytes located at the wound edge. As by light microscopy,  
197 EM images showed that FAs connected to actin bundles were distributed further within the protrusion  
198 in case of  $\alpha$ TAT1 cells as compared to a highly organised and parallel set of FAs at the leading edge of  
199 control cells (Fig. 3d). From the high magnification views of FAs in the control cells, microtubules were  
200 often seen along actin cables reaching FAs (Fig. 3d, marked with white arrows in i.1). Intermediate  
201 filaments were also clearly visible, intertwined with the actin filaments at FAs (Fig. 3d, marked with  
202 yellow arrows in i. 2 and i. 3). In  $\alpha$ TAT1 cells, the actin bundles near FAs were strikingly thinner than  
203 those in controls (Fig. 3d). We consistently observed a lack of microtubules and intermediate filaments  
204 associated with FAs in  $\alpha$ TAT1-depleted cells (Fig. 3d). All these results strongly support a role for  $\alpha$ TAT1  
205 in the cytoskeletal organisation at FAs in astrocytes. We then tested the effects of microtubule  
206 acetylation on the cytoskeletal organisation by treating HUVECs and astrocytes plated on soft substrates  
207 with Tubacin to increase microtubule acetylation. In Tubacin-treated cells, we observed prominently  
208 larger actin cables, increased Myosin-IIa filaments, together with larger and more peripheral FAs (Fig. 3e  
209 and Extended Data Fig. 3b), reminiscent of the phenotype observed in astrocytes plates on stiff  
210 substrates (Fig. 3f), confirming that microtubule acetylation regulates actomyosin organization.

211

212

213

214 **Microtubule acetylation increases actomyosin contractility via GEF-H1 and Rho**

215

216 One major impact of mechanosensing is the adaptation of traction forces to the rigidity of the  
217 substrate<sup>34</sup>. We thus investigated whether microtubule acetylation might affect traction forces by  
218 plating control or  $\alpha$ TAT1-depleted astrocytes on crossbow-shaped micropatterned hydrogels. By  
219 traction force microscopy, we observed that  $\alpha$ TAT1 depletion resulted in lower traction force production  
220 on 40 kPa substrates (Fig. 4a and 4b). In contrast, overexpression of GFP- $\alpha$ TAT1 increased traction  
221 energies and forces and also rescued the effect observed on  $\alpha$ TAT1 knockdown (si $\alpha$ TAT1 + GFP- $\alpha$ TAT1;  
222 Fig. 4a and 4b) when astrocytes were plated on 40 kPa. In addition, Tubacin-treated astrocytes on soft 2  
223 kPa hydrogels showed increased traction energies and forces, comparable to control astrocytes plated  
224 on 40 kPa (Fig. 4c). We also studied the effects of microtubule acetylation on traction forces in Tubacin-  
225 treated HUVECs plated on soft 2 kPa substrates. Similar to astrocytes, increased microtubule acetylation  
226 using Tubacin resulted in higher traction energies and forces in HUVECs (Fig. 4d). Thus, the level of  
227 microtubule acetylation dictates traction forces exerted on the substrate through FAs. This further  
228 illustrates the essential role of the mechanosensitive regulation of microtubules in force transmission.

229 The crucial role of microtubule acetylation in the controlling cytoskeletal organisation and traction  
230 forces led us to further investigate the molecular mechanisms involved in this process. We focused on  
231 RhoA, a small G protein of the Rho family, well-known for promoting stress fibre formation and  
232 actomyosin contractility, via its effector ROCK and MLC phosphorylation. Pulldown of GTP-bound active  
233 RhoA using GST-Rhotekin beads showed that  $\alpha$ TAT1 depletion reduced RhoA activity (Fig. 4e),  
234 suggesting that microtubule acetylation may promote actomyosin contractility by activating RhoA. RhoA  
235 activation is mediated by Guanine nucleotide exchange factors (GEFs)<sup>35</sup>. Amongst these GEFs, GEF-H1  
236 (also known as ARHGEF2) is a microtubule-bound RhoGEF which, when released from microtubules  
237 triggers the Rho-ROCK signalling cascade and cell contractility<sup>36,37</sup>. Previously, substrate stiffness was  
238 suggested to correlate with GEF-H1 activity and actomyosin contractility<sup>38</sup>. In addition, GEF-H1 was

239 recently shown to be controlled by the interaction of microtubules with integrin-mediated adhesions<sup>39</sup>,  
240 leading us to investigate whether integrin-mediated microtubule acetylation could affect the association  
241 of GEF-H1 with microtubules. In control astrocytes plated on rigid glass coverslips, GEF-H1 localised  
242 partially (approximately 42%) on microtubules but also in the cytosol, a localisation that corresponds to  
243 the active/released GEF- H1 (Fig. 5a and Extended Data Fig. 5a)<sup>40</sup>. In contrast, in  $\alpha$ TAT1-depleted cells,  
244 GEF-H1 was predominantly localised on microtubules (approximately 60%; Fig. 5a and Extended Data  
245 Fig. 5a). Tubacin treatment of  $\alpha$ TAT1-depleted cells led to the release of GEF-H1 into the cytosol,  
246 rescuing the effect of  $\alpha$ TAT1 depletion and confirming the role of microtubule acetylation in the GEF-H1  
247 localisation (Fig. 5a and Extended Data Fig. 5a). In control HUVECs (which exhibit relatively low levels of  
248 acetylated tubulin) GEF-H1 was mostly bound to microtubules (approximately 50%; Fig. 5b). Like in  
249 astrocytes, the treatment of HUVECs with Tubacin resulted in the release of GEF-H1 into the cytoplasm,  
250 with only 38% of GEF-H1 colocalising with microtubules (approximately 38%; Fig. 5b). GEF-H1  
251 association with microtubules was confirmed using GFP-immunoprecipitation experiments using HEK  
252 cells transfected with GFP-Ctl or GFP-GEF-H1 (Fig. 5c). Like Nocodazole treatment which leads to the  
253 depolymerisation of microtubules, Tubacin treatment (which increases microtubule acetylation)  
254 abolished the binding of GEF-H1 to microtubules (Fig. 5c). Altogether, these results show that  
255 microtubule acetylation promotes the release of GEF-H1 from microtubules into the cytoplasm.

256

257 We then tested whether substrate rigidity and  $\alpha$ TAT1 play a role in the association of GEF-H1 with  
258 microtubules. Astrocytes plated soft 2 kPa substrates exhibit a higher microtubule-bound portion of  
259 GEF-H1 as compared to cells on stiff 48 kPa gels (Fig. 5d and Extended Data Fig. 5b). In  $\alpha$ TAT1-depleted  
260 cells plated on stiff substrates, GEF-H1 was found predominantly bound to microtubules, mimicking the  
261 phenotype observed in cells plated on soft substrates (Fig. 5d and Extended Data Fig. 5b). These results

262 strongly suggest that rigidity-dependent microtubule acetylation contributes to mechanotransduction  
263 by enabling RhoA activation and actomyosin contractility.

264

## 265 **Microtubule acetylation modulates mechanosensitive cell migration by tuning** 266 **mechanotransduction at focal adhesions**

---

267

268 The involvement of microtubule acetylation in mechanotransduction and in the mechanosensitive  
269 regulation of FAs and actomyosin contractility led us to investigate its influence on cell migration, which  
270 has often been described as a mechanosensitive cellular response<sup>2,41</sup>. To this end, we developed a  
271 collective migration assay on hydrogels, where microdropping a small amount of a chemical (sodium  
272 hydroxide) induced a circular wound in the cell monolayer (Fig. 6A, Supplementary Video 3). Sodium  
273 hydroxide treatment did not noticeably alter the hydrogel properties (see Methods). Wild-type  
274 astrocytes migrated significantly slower on 2 kPa gels than on 48 kPa gels (Fig. 6B, Supplementary Video  
275 4), implying that astrocyte migration speed is affected by substrate rigidity. Most importantly,  $\alpha$ TAT1  
276 depletion abolished the increase of cell speed observed on stiff 48 kPa gels (Fig. 6C, Supplementary  
277 Video 5), so that the migration speed of  $\alpha$ TAT1-depleted cells plated on 48 kPa was similar to that of  
278 control and  $\alpha$ TAT1-depleted cells on 2 kPa substrates. In addition, the effects of  $\alpha$ TAT1 depletion in cells  
279 plated on 48 kPa gels is in line with our previous results described on the role of  $\alpha$ TAT1 during collective  
280 migration on glass coverslips<sup>13</sup>. Thus, we demonstrate that microtubule acetylation is required for the  
281 mechanosensitive regulation of astrocyte collective migration.

282

## 283 **Discussion**

---

284

285 Our results show that microtubules are regulated in response to substrate rigidity sensing and in  
286 turn, play a key role in mechanotransduction by participating in mechanosensitive cellular responses,

287 including translocation of the transcriptional coactivator YAP, focal adhesion distribution, actomyosin  
288 contractility, generation of traction forces and cell migration (Fig. 6d). Our results point to a mechanism  
289 by which Talin-mediated mechanosensing downstream of integrin-mediated signalling (Fig. 6d-i)  
290 controls the recruitment of  $\alpha$ TAT1 to FAs (Fig. 6d-ii) and induces microtubule acetylation (Fig. 6d-iii). We  
291 show that  $\alpha$ TAT1 interacts with Talin and that, on rigid substrates, Talin is required for the recruitment  
292 of  $\alpha$ TAT1 to FAs, and for the acetylation of microtubules (Fig. 6d-ii). Although we do not have any clear  
293 evidence of a direct interaction of Talin with  $\alpha$ TAT1, the  $\beta_1$ -integrin- and actomyosin-dependent  
294 association of  $\alpha$ TAT1 with Talin suggest that tension-induced changes in Talin conformation may be  
295 involved in inducing  $\alpha$ TAT1 recruitment to FAs and microtubule acetylation.

296

297 How  $\alpha$ TAT1 enters the lumen of microtubules still remains unclear although one can speculate that  
298  $\alpha$ TAT1 accesses the lumen through microtubule lattice defects or through the open ends<sup>21</sup>. Growing  
299 microtubule ends are often seen in close proximity to FAs at the leading edge of migrating cells<sup>8</sup>  
300 (Extended Data Fig. 5C). It is very likely that, like other FA-associated proteins, a large proportion of  
301 talin-associate  $\alpha$ TAT1 rapidly exchange with a cytosolic pool<sup>42</sup>. This lead us to propose a model in which  
302 the increased interaction of  $\alpha$ TAT1 with talin increases the local concentration of  $\alpha$ TAT1 and facilitates  
303 its entry in the microtubule lumen through microtubule open ends in the vicinity of adhesions (Fig. 6D-  
304 iii; Extended Data Fig. 5C).

305

306 We show that microtubule acetylation reorganises the actomyosin network and promotes traction  
307 forces. Therefore, we propose a feedback mechanism involving a crosstalk between microtubules and  
308 actin wherein, actomyosin-dependent mechanosensing promotes microtubule acetylation which, in  
309 turn, facilitates the release of GEF-H1 from microtubules into the cytosol (Fig. 6D-iv) to increase RhoA  
310 activity (Fig. 6D-v), cell contractility (Fig. 6D-vi) and traction forces (Fig. 6D-vii). It was recently shown

311 that uncoupling microtubules from FAs results in a similar release of microtubule-bound GEF-H1 into the  
312 cytosol<sup>39</sup>, which then triggers myosin IIA assembly and increased cell contractility through RhoA.  
313 Suppression of RhoA activity in the absence of  $\alpha$ TAT1 might be due to the sequestering of GEF-H1 by  
314 non-acetylated microtubules. Whether microtubule acetylation directly or indirectly induces the release  
315 of GEF-H1 remains unclear. One can speculate that acetylation of Lysine 40 changes the conformation of  
316  $\alpha$ -tubulin and modifies the binding site for GEF-H1, thereby, inducing its release from microtubules.  
317 Alternatively, acetylation might change the mechanical properties of the microtubule lattice and affect  
318 its curvature<sup>41,42</sup>, which would in turn facilitate the release of GEF-H1 from microtubules. It is also  
319 possible that any of the previous mechanisms affect a binding of a partner of GEF-H1, which alters GEF-  
320 H1 conformation (via phosphorylation for instance) and promote its release into the cytosol.  
321 Interestingly, microtubule acetylation also affects the association of intermediate filaments with actin  
322 bundles at FAs. Since intermediate filaments have also been involved in the control of FA dynamics,  
323 actomyosin contractility as well as GEF-H1 activity<sup>32,40</sup>, the microtubule-actin interplay described here  
324 may also involve intermediate filaments, whose role in mechanotransduction is still elusive.

325

326 In response to substrate rigidity sensing, cells adapt essential functions such as migration<sup>43</sup>. In the  
327 absence of  $\alpha$ TAT1, cells plated on stiff substrates produce less traction forces and migrate slower ([Fig.](#)  
328 [6d-viii](#)). The relationship between forces and migration can be considered counter-intuitive for single  
329 cell migration where traction forces appear to correlate with migration speed; and contractile forces are  
330 required for migration but exaggerated traction forces tend to slow or even stop migration<sup>44</sup>. In fact,  
331 measurements of traction forces exerted by astrocytes plated on substrates of various rigidities shows  
332 that there is a rigidity optimum (around 50 kPa), at which the forces are maximal ([Extended Data Fig.](#)  
333 [5d](#)). When looking at microtubule acetylation, actomyosin contractility, or cell migration, it is clear that  
334 all of them increase up to about 48kPa but then reach a plateau or even decrease when cells are plated

335 on glass, indicative of a non-monotonous response. In collective cell migration, the distribution of forces  
336 within the migrating monolayer, more than the intensity itself, is crucial for the efficient control of  
337 collective cell migration. Also, collective cell migration relies on the transmission of forces between the  
338 leaders and followers. Cell-cell junctions not only transmit forces between cells but help maintain the  
339 integrity of the monolayer<sup>26,45</sup>, which improves collective and directed cell migration. Alteration of  
340 microtubule acetylation did not induce any detachment of leader cells from followers and did not affect  
341 directionality or persistence of migration<sup>13</sup>. Therefore, we propose a model in which, on stiff substrates,  
342 increased microtubule acetylation would trigger higher traction forces in leader cells, which would  
343 transmit these pulling forces to followers and increase collective migration speed. Microtubule  
344 acetylation may also affect cell migration by controlling FA dynamics. We have previously demonstrated  
345 that microtubule acetylation promotes the fusion of Rab6-dependent post-Golgi carriers at FAs and  
346 increases FA turnover<sup>13</sup>, such that they are continuously renewed at the front of leader cells. Depletion  
347 of  $\alpha$ TAT1 (as that of Rab6) alters the distribution of FAs in migrating cells<sup>13</sup>. The change in FA distribution  
348 between the cell center and the cell periphery suggests that rigidity-induced acetylation of microtubules  
349 may promote FA turnover during cell spreading, thereby, excluding them from the cell center. We  
350 speculate that the increase in FA turnover together with the increase in cell contractility participate in  
351 strengthening the traction forces exerted on FAs concentrated at the leader cell wound edge and  
352 improve astrocyte collective migration (Fig. 6d-viii).

353

354 In conclusion, our results depict a crosstalk between the actin and microtubule cytoskeletal  
355 networks (Fig. 6d), whereby microtubule acetylation, downstream of rigidity-dependent integrin-  
356 mediated signalling, alters actomyosin contractility as well as focal adhesion distribution and dynamics  
357 to promote mechanosensitive migration of astrocytes, thus closing a crucial feedback loop governing  
358 mechanotransduction at FAs (Fig. 6d).



359  
360  
361  
362  
363  
364  
365  
366  
367  
368  
369  
370  
371  
372  
373  
374  
375  
376  
377  
378  
379  
380  
381  
382  
383  
384

## Methods

---

### Cell culture

Primary astrocytes were obtained from E17 rat embryos<sup>12</sup>. Use of these animals is in compliance with ethical regulations and has been approved from the Prefecture de Police and Direction départementale des services vétérinaires de Paris. Astrocytes were grown in 1g/L glucose DMEM supplemented with 10% FBS (Invitrogen, Carlsbad, CA), 1% penicillin-streptomycin (Gibco) and 1% Amphotericin B (Gibco) at 5% CO<sub>2</sub> and 37°C. Human umbilical vein endothelial cells (HUVECs) were cultured in EGM-2 BulletKit media (Lonza, catalogue no. CC-3162).

### Cell nucleofection

Astrocytes were transfected with Lonza glial transfection solution and electroporated with a Nucleofector machine (Lonza). Cells were then plated on appropriate supports previously coated with poly-L-Ornithine (Sigma). Experiments are carried out 3 or 4 days post-transfection and comparable protein silencing was observed. siRNAs were used at 1 nmol and DNA was used at 5 µg. siRNA sequences used were:

Luciferase (control) UAAGGCUAUGAAGAGAUAC; αTAT1 rat (siαTAT1-1): 5'-ACCGACACGUUAAUUUAUGU-3' and 5'-UUCGAAACCGCAGGAACG-3'; αTAT1 rat (siαTAT1-2): 5'-UAAUGGAUGUACUCAUUCA-3' and 5'-UCAUGACUAAUUGUAGAUGA-3'; Talin-1 rat (siTalin1): 5'-GGGACACCAUGGAGUACAGAA-3', 5'-GACCCCCACUCCAGGAUAAU-3', 5'-GCUGGAAGCUGUGGAUAACCU-3', and 5'-GACCUCCACCCCUGAAGAUUU-3'; β<sub>1</sub> integrin (AUUGCCAGAUGGAGUAACA).

Constructs used were: GFP-αTAT1 and GST-αTAT1 (gift from Philippe Chavier, Institut Curie and Guillaume Montagnac, Institut Gustave Roussy) and mCherry-vinculin. siαTAT1-1 and siαTAT1-2 are

385 pools of two siRNAs each. For all experiments, si $\alpha$ TAT1-2 has been used due to better knockdown  
386 efficiency as seen in Extended Fig. 1a and previously characterized in<sup>13</sup>. A few major experiments have  
387 been carried out with si $\alpha$ TAT1-1 and the results are shown in the respective extended data figures.

#### 388 **Cell treatment**

389 Cells were treated with 5-10  $\mu$ M Tubacin (Sigma SMLOO65) or 10  $\mu$ M Niltubacin (negative control for  
390 Tubacin; Enzo Life Sciences) or DMSO (control) were added cells (3 h treatment for HUVECs; 6 h  
391 treatment for astrocytes). Similarly, RGD peptide (Enzo Life Sciences) and RGE Control peptide (Enzo Life  
392 Sciences) were added prior to wounding. ROCK inhibitor, Y-27632, and MnCl<sub>2</sub> (1  $\mu$ M) were added 6 h  
393 after wounding and 2 h before fixation. For TIRF experiments, 10  $\mu$ M Nocodazole or Y-27632 were  
394 added after 10 min of acquisition. For pull-downs, 10  $\mu$ M Nocodazole or Y-27632 were added 1 h before  
395 cell lysis.

#### 396 **Preparation of homogenously coated polyacrylamide hydrogels**

397 Protocol to prepare polyacrylamide hydrogels was adapted from<sup>41,46,47</sup>. Coverslips were plasma cleaned  
398 for 3 min and silanised for 10 min using a solution of 1% (v/v) 3-(trimethoxysilyl)propyl methacrylate and  
399 1% (v/v) acetic acid in ethanol. Coverslips were then washed twice with absolute ethanol and dried. A  
400 solution of polyacrylamide (proportions of acrylamide and bisacrylamide in the solution define the  
401 rigidity of the hydrogel) was prepared. 2.5  $\mu$ l 10% APS and 0.25  $\mu$ l TEMED was added and mixed well  
402 with the solution. A 50  $\mu$ l drop of the solution was added over each coverslip (20x20 mm) and  
403 immediately, an 18x18 mm coverslip was placed gently over the solution. The solution was allowed to  
404 polymerise for 1 h at room temperature. HEPES was added over the coverslips to detach the top glass.  
405 The polymerised gel was then activated under UV for 5 min using Sulpho-SANPAH and washed with  
406 HEPES twice. The hydrogels were then coated with 100  $\mu$ g/ml of rat tail collagen I overnight at 4°C. The  
407 excess collagen was washed once with PBS and approximately 5 x 10<sup>4</sup> cells/ml were plated on hydrogels.

#### 408 **Micropatterning**

409 Coverslips were plasma-cleaned for 45 s and incubated with 0.1 mg/ml poly-L-lysine/polyethylene glycol  
410 (PLL-PEG) diluted in 10 mM HEPES for 30 min at room temperature. Excess of PLL-PEG was allowed to  
411 slide down by gravity, and the coverslips were dried and stored at 4°C overnight before printing.  
412 Micropatterns were printed on previously prepared PLL-PEG coverslips for 3 min with specifically  
413 designed chrome masks and coated with 50:50 v/v fibronectin/fibrinogen mixture (20 µg/ml each)  
414 diluted in fresh NaHCO<sub>3</sub>, pH 8.3, 100 mM, for 30 min at room temperature. Micropatterned coverslips  
415 were washed thrice in NaHCO<sub>3</sub> and used immediately for transfer on hydrogels. Plated cells  
416 (approximately 6 x 10<sup>4</sup> cells/ml) were allowed to adhere for 16 h before imaging/fixation. Crossbow  
417 patterns have an area of ~2500 µm<sup>2</sup>.

#### 418 **Traction force experiments on micropatterned substrates**

419 After printing and coating micropatterned coverslips, gel mixtures were prepared as follows: 40.4 kPa –  
420 100 µl 40% acrylamide, 120 µl 2% bisacrylamide, 280 µl water (final concentration of 8% acrylamide and  
421 0.48% bisacrylamide in water); 2.61 kPa – 50 µl 40% acrylamide, 25 µl 2% bisacrylamide, 425 µl water  
422 (final concentration of 8% acrylamide and 0.048% bisacrylamide in water). 5 µl of fluorescent  
423 microbeads (FluoSpheres; Molecular Probes) were incubated with 0.1 mg/ml PLL-PEG on a rotator for 1  
424 h at 4°C prior to mixing with the gel mixture. The PLL-PEG coated beads were washed and centrifuged  
425 thrice at 1000 rpm for 10 min with 10 mM HEPES. These beads were then mixed with 165 µl of the gel  
426 mixture. After adding 1 µl APS and 1 µl TEMED, the solution was added as a 25 µl drop on a silanised  
427 20x20 mm coverslip. The protein-coated micropatterned coverslip was then gently placed on the gel  
428 mixture. The solution was allowed to polymerize for 25 min at room temperature. After detaching the  
429 micropatterned glass from the polymerized gel, 6 x 10<sup>4</sup> cells/ml were plated on the gels and allowed to  
430 adhere and spread for 16 h before TFM experiments. Stacks of single micropatterned cells were  
431 acquired before and after trypsin treatment. Acquisitions were performed with a Nikon Eclipse Ti-E  
432 epifluorescence inverted microscope, with a 40× 1.49 NA air objective equipped with a pco.edge sCMOS

433 camera and Metamorph software. Cells were maintained at 5% CO<sub>2</sub> and 37°C in normal astrocyte  
434 medium during acquisition.

#### 435 **Migration assays**

436 In vitro wound healing assays: cells were plated on appropriate supports (dishes, plates, coverslips or  
437 glass-bottom MatTek) and grown to confluence. The cell monolayer was scratched with a p200 pipette  
438 tip to induce migration and imaged during 8h.

439 Migration on soft substrates: cells were plated on hydrogels of different rigidities in 6-well glass bottom  
440 plates (MatTek) and allowed to grow for 72 h after transfection before creating a chemical wound. 0.05  
441 M NaOH was gently dropped on the cells using a microinjector. NaOH is used to instantly kill and detach  
442 cells localized in a region of a few hundred microns. The NaOH is added with a microinjector which  
443 delivers a fraction of a nanoliter of NaOH (0.05M) on a cell monolayer, which immediately mixes with 2  
444 ml of culture medium that is present in the culture dish. The dead cells and debris were gently washed  
445 away using PBS. Fresh medium was added to the cells. Cells were placed on the microscope for live  
446 imaging. In these conditions, the hydrogel is only very locally and briefly exposed to the chemical. As  
447 cells migrate into this space (wounded area of the monolayer), the fibronectin coating and the surface  
448 of the hydrogel remains intact with negligible and unnoticeable changes. NaOH treatment did not affect  
449 the weight of the gel -indicative of gel swelling-; it did not induce any detectable bead movements –  
450 indicative of gel contraction or expansion of the gel-, nor did it affect the traction forces of cells,  
451 indicating that cells did not sense any difference in substrate rigidity. Acquisition was started 30 min  
452 after wounding. Supplementary Videos were acquired with a Zeiss Axiovert 200M or a Nikon Eclipse Ti-E  
453 epifluorescence inverted microscope with cells maintained at 5% CO<sub>2</sub> and 37°C. All images were  
454 acquired with dry objective 10X 0.45 NA and an EMCCD camera/pco.edge sCMOS camera and  
455 Metamorph software. Images were acquired every 15 min for 24 h. Nuclei of leader cells were manually  
456 tracked with Fiji software (Manual Tracking plugin).

457 **Immunostaining**

458 Cells were fixed with cold methanol for 3 min at -20°C, or 4% warm PFA, or 4% PFA + 0.2%  
459 glutaraldehyde + 0.25% Triton X-100 for 10 min at 37°C. After fixation with PFA, glutaraldehyde and  
460 triton, free aldehyde groups were quenched with a solution of 1 mg/ml sodium borohydride (Sigma-  
461 Aldrich) freshly added to cytoskeletal buffer (10 mM MES or MOPS, 150 mM NaCl, 5 mM EGTA, 5 mM  
462 MgCl<sub>2</sub>, 5 mM glucose, pH 6.1) for 10 min on ice. Cells were permeabilised for 5 min with 0.1% Triton in  
463 case of PFA fixation. Coverslips were blocked for 1 h with 5% BSA in PBS. The same solution was used for  
464 primary and secondary antibody incubation for 1 h. Nuclei were stained for DAPI and coverslips were  
465 mounted with Prolong Gold.

466 Antibody anti-Acetylated Tubulin (1:10000; clone 6-11B-1, mouse monoclonal, T-6793 Sigma Aldrich or  
467 1:200; clone 6-11B-1, ab24610, Abcam), anti-Poly-Glu Tubulin (1:1000; AbC0101, ValBiotech), anti- $\alpha$ -  
468 Tubulin (1:1000; MCA77G, rat, Biorad), anti-Paxillin (1:500; 610051, mouse monoclonal, lot 5246880;  
469 BD; and ab32084, rabbit monoclonal, clone Y133 and lot GR215998-1; Abcam), anti-Talin (1:1000;  
470 T3287, mouse monoclonal, clone 8D4, lot 035M4805V; Sigma-Aldrich), anti-GEF-H1 (1:100; ab155785,  
471 Abcam), Alexa fluor 647 Phalloidin (1:2000; 176759, lot GR278180-3; Abcam or 1:300; Thermo Fisher  
472 Scientific), anti-Vimentin (1:200; V6630, mouse monoclonal lot 10M4831; Sigma-Aldrich), anti-pMLC  
473 (1:1000; 3675S, S19, mouse, Cell signalling), anti-Myosin IIA (1:1000; non-muscle, M8064, rabbit  
474 polyclonal, Sigma-Aldrich), anti-Vinculin (1:400; V9131, Sigma-Aldrich). Secondary antibodies were Alexa  
475 Fluor 488 donkey anti-rabbit (711-545-152), Rhodamine (TRITC) donkey anti-rabbit (711-025-152),  
476 Alexa Fluor 647 donkey anti-rabbit (711-695-152), Alexa Fluor 488 donkey anti-mouse (715-545-151),  
477 Rhodamine (TRITC) donkey anti-mouse (715-025-151), Alexa Fluor 647 donkey anti-rat (711-605-152),  
478 and Alexa Fluor 488 donkey anti-rat (712-545-153); all from Jackson ImmunoResearch. Images were  
479 acquired with a Leica DM6000 microscope equipped with 40X 1.25 NA or 63X 1.4 NA objectives and

480 recorded on a CCD camera with a Leica software, or imaged at the basal plane using Yokogawa CSU-W1,  
481 Nikon TiE Spinning disk confocal microscope, at 100x magnification.

#### 482 **TIRF microscopy**

483 Acquisitions were performed with a Nikon Eclipse Ti-E epifluorescence inverted microscope, with a 60x  
484 1.49 NA oil objective equipped with a pco.edge sCMOS camera with Metamorph software. Cells were  
485 maintained at 5% CO<sub>2</sub> and 37°C in normal astrocyte medium. After acquiring a 15 min movie of GFP-  
486 αTAT1 and mCherry-vinculin, Nocodazole or Y27 were added and images were acquired every 2 min for  
487 1 h.

#### 488 **Transmission electron microscopy**

489 Adherent migrating astrocytes plated on glass coverslips were disrupted by sonication as described  
490 previously<sup>48</sup>. Coverslips were unroofed by scanning the coverslip with rapid sonicator pulses in KHMgE  
491 buffer (70 mM KCl, 30 mM HEPES, 5 mM MgCl<sub>2</sub>, 3 mM EGTA, pH 7.2). Paraformaldehyde  
492 2%/glutaraldehyde 2%-fixed cells were further sequentially treated with 0.5% OsO<sub>4</sub>, 1% tannic acid and  
493 1% uranyl acetate prior to graded ethanol dehydration and Hexamethyldisilazane substitution (HMDS,  
494 Sigma-Aldrich). Dried samples were then rotary-shadowed with 2 nm of platinum and 5-8 nm of carbon  
495 using an ACE600 high vacuum metal coater (Leica Microsystems). Platinum replicas were floated off the  
496 glass by 5% hydrofluoric acid, washed several times by floatation on distilled water, and picked up on  
497 200 mesh formvar/carbon-coated EM grids. The grids were mounted in a eucentric side-entry  
498 goniometer stage of a transmission electron microscope operated at 80 kV (Philips, model CM120) and  
499 images were recorded with a Morada digital camera (Olympus). Images were processed in Adobe  
500 Photoshop to adjust brightness and contrast and presented in inverted contrast.

#### 501 **Image analysis**

502 Normalised mean intensity levels of acetylated and detyrosinated tubulin for immunofluorescence  
503 images were calculated as shown in equation 1:

504

1

$$\text{Ratio of acetyl or deetyr tubulin level} = \frac{\text{Acetyl/deetyr tubulin intensity}}{\text{Total tubulin intensity}}$$

505 YAP nuclear/cytoplasmic ratio was calculated as shown in equation 2:

506

2

$$\text{YAP nuclear to cytoplasmic ratio} = \frac{\text{Intensity of YAP in the nucleus}}{\text{Intensity of YAP in the cytoplasm}}$$

507 FA density was calculated as shown in equation 3:

508

3

$$\text{FA density} = \frac{\text{Number of FAs in the region}}{\text{Area of the region}}$$

509 Different regions of cells (entire cell, cell periphery-8  $\mu\text{m}$ , 8  $\mu\text{m}$ -16  $\mu\text{m}$ , 16  $\mu\text{m}$ -cell center) were analysed

510 as depicted in Extended Data Fig. 2d.

511 For migration assays, nuclei of cells were manually tracked to determine the speed directionality and

512 persistence of migration using the following formulae:

513 Mean velocity ( $v$ ), persistence ( $p$ ) and directionality ( $d$ ) of cell migration are calculated shown in514 equations 4-6: for a given  $(x, y)$  coordinate of leading cell nucleus,

515

4

$$v = \frac{\sum \vartheta}{n}$$

516

5

$$p = \frac{\sqrt{[(x_{24} - x_0)^2 + (y_{24} - y_0)^2]}}{\sum \sqrt{[(x_n - x_{n-1})^2 + (y_n - y_{n-1})^2]}}$$

517

6

$$d = \frac{|(x_0 - x_{24})|}{\sum \sqrt{[(x_n - x_{n-1})^2 + (y_n - y_{n-1})^2]}}$$

518 where  $n$  is the number of time points acquired and  $v$  is cell velocity.

519 Analysis of TFM on micropatterns was performed with a custom-designed macro in Fiji based on work by  
520 <sup>49</sup>. The topmost planes of beads before and after trypsinisation were selected and aligned using a  
521 normalized cross-correlation algorithm (Align Slices in Stack plugin). The displacement field was  
522 computed from bead movements using particle image velocimetry (PIV). Parameters for the PIV were  
523 three interrogation windows of 128, 64, and 32 pixels with a correlation of 0.60. Traction forces were  
524 calculated from the displacement field using Fourier transform traction cytometry and a Young's  
525 modulus of 40 kPa or 2 kPa, a regularization factor of  $10^{-9}$ , and a Poisson ratio of 0.5.

526 For the localisation of GEF-H1 on microtubules, the percentage GEF-H1 on microtubules was calculated  
527 as shown in equation 7:

528 7

$$\text{Percentage intensity of GEFH1 localisation on MT} = \frac{\text{Intensity of GEFH1 on microtubules}}{\text{Intensity of GEFH1 outside microtubules}} \times 100$$

### 529 **Immunoprecipitations and pulldown assays**

530 Cell lysates were prepared by scraping cells in 1X lysis buffer (10X buffer recipe: 50 mM Tris pH 7.5,  
531 triton 20%, NP40 10%, 2 M NaCl with Complete protease inhibitor tablet (Roche, Indianapolis, IN)) and  
532 centrifuged for 30 min at 13,000 rpm 4°C to pellet cell debris. Soluble detergent extracts were incubated  
533 with GFP-Trap agarose beads (Chromotek, GTP-20) for immunoprecipitation and with GST or GST-  
534  $\alpha$ TAT1 beads for 2 hr at 4°C prior to washing three times with wash buffer (50 mM Tris pH 7.5, 150 mM  
535 NaCl, 0.1% triton, 1 mM EDTA, 2.5 mM MgCl<sub>2</sub>). The resin was then mixed with Laemmli buffer and used  
536 for western blot and mass spectrometry analysis. HEK293 cells were used for mass spectrometry  
537 analysis in order to have enough amount of protein from cells expressing  $\alpha$ TAT1.

### 538 **Mass spectrometry**



539 Proteins on beads were washed twice with 100  $\mu$ L of 25 mM  $\text{NH}_4\text{HCO}_3$  and we performed on-beads  
540 digestion with 0.2  $\mu$ g of trypsin/LysC (Promega) for 1 h in 100  $\mu$ L of 25 mM  $\text{NH}_4\text{HCO}_3$ . Sample were  
541 then loaded onto a homemade C18 StageTips for desalting. Peptides were eluted using 40/60  
542 MeCN/ $\text{H}_2\text{O}$  + 0.1% formic acid and vacuum concentrated to dryness. Online chromatography was  
543 performed with an RSLCnano system (Ultimate 3000, Thermo Scientific) coupled to an Orbitrap Fusion  
544 Tribrid mass spectrometer (Thermo Scientific). Peptides were trapped on a C18 column (75  $\mu$ m inner  
545 diameter  $\times$  2 cm; nanoViper Acclaim PepMapTM 100, Thermo Scientific) with buffer A (2/98 MeCN/ $\text{H}_2\text{O}$   
546 in 0.1% formic acid) at a flow rate of 4.0  $\mu$ L/min over 4 min. Separation was performed on a 50 cm  $\times$  75  
547  $\mu$ m C18 column (nanoViper Acclaim PepMapTM RSLC, 2  $\mu$ m, 100 $\text{\AA}$ , Thermo Scientific) regulated to a  
548 temperature of 55 $^\circ$ C with a linear gradient of 5% to 25% buffer B (100% MeCN in 0.1% formic acid) at a  
549 flow rate of 300 nL/min over 100 min. Full-scan MS was acquired in the Orbitrap analyzer with a  
550 resolution set to 120,000 and ions from each full scan were HCD fragmented and analyzed in the linear  
551 ion trap.

552 For identification, the data was searched against the Homo sapiens (UP000005640) SwissProt database  
553 using Sequest<sup>HF</sup> through proteome discoverer (version 2.2). Enzyme specificity was set to trypsin and a  
554 maximum of two missed cleavage site were allowed. Oxidized methionine, N-terminal acetylation, and  
555 carbamidomethyl cysteine were set as variable modifications. Maximum allowed mass deviation was set  
556 to 10 ppm for monoisotopic precursor ions and 0.6 Da for MS/MS peaks. The resulting files were further  
557 processed using myProMS<sup>50</sup> v3.6 (work in progress). FDR calculation used Percolator and was set to 1%  
558 at the peptide level for the whole study. The label free quantification was performed by peptide  
559 Extracted Ion Chromatograms (XICs) computed with MassChroQ version 2.2<sup>51</sup>. For protein  
560 quantification, XICs from proteotypic peptides shared between compared conditions (TopN matching)  
561 with no missed cleavages were used. Median and scale normalization was applied on the total signal to  
562 correct the XICs for each biological replicate. To estimate the significance of the change in protein

563 abundance, a linear model (adjusted on peptides and biological replicates) was performed and p-values  
564 were adjusted with a Benjamini–Hochberg FDR procedure with a control threshold set to 0.05. Up-  
565 regulated proteins with at least 3 proteotypic peptides (fold change > 1.5 and p-value < 0.05) and the  
566 unique proteins identified only in the GFP- $\alpha$ TAT1 were used for gene ontology (GO) enrichment analysis  
567 by using GO::TermFinder tools (10.1093/bioinformatics/bth456) through myProMS.

568 The mass spectrometry proteomics data have been deposited to the ProteomeXchange Consortium via  
569 the PRIDE<sup>52,53</sup> partner repository with the dataset identifier PXD015871 (username:  
570 reviewer89842@ebi.ac.uk; password: EC4DSdRf; project name: Potential interactors of alpha-tubulin  
571 acetyltransferase 1 ( $\alpha$ TAT1/MEC17).

#### 572 **Rho activation assay**

573 Rho activation assay was performed using a RhoA Pull-down Activation Assay Biochem Kit from  
574 Cytoskeleton Inc (BK036-S). In short, cells were lysed in ice-cold Cell Lysis Buffer plus 1x protease  
575 inhibitor cocktail. Cells were centrifuged at 10,000 g at 4°C for 10 min to pellet cell membranes and  
576 insoluble material. Part of the supernatant was stored as input for western blot. The remaining  
577 supernatant was divided equally into two parts (300-800  $\mu$ g protein/tube). 1/15<sup>th</sup> the volume of Loading  
578 Buffer was added to each tube (final conc. 15 mM). Then, 1/100<sup>th</sup> the volume of GTP $\gamma$ S was added to  
579 one of the tubes and used as positive control (final conc. 0.2 mM). All tubes were incubated at room  
580 temperature for 15 min. The reaction was stopped by adding 1/10<sup>th</sup> the volume of STOP Buffer to all  
581 tubes (final conc. 60 mM).

582 Rhotekin-RBD (50  $\mu$ g) beads were resuspended and added to the tubes. Tubes were rotated at 4°C for 1  
583 h and centrifuged at 5000 g at 4°C for 3 min. Beads were washed with 500  $\mu$ l each of Wash Buffer. 10-20  
584  $\mu$ l of Laemmli sample buffer was added to each tube.

## 585 **Western blot**

586 Cells lysates were obtained with Laemmli buffer composed of 60 mM Tris-HCl pH6.8, 10% glycerol, 2%  
587 SDS and 50 mM DTT with the addition of anti-protease (cOmplete cocktail, Roche 11 873 588 001).  
588 Samples were boiled 5 min at 95°C before loading on polyacrylamide gels. Transfer occurred at 100V for  
589 1 h on nitrocellulose membranes. Membranes were blotted with TBST (0.2% Tween) and 5% milk and  
590 incubated 1 h with the primary antibody and 1 h with HRP-conjugated secondary antibody. Bands were  
591 revealed with ECL chemoluminescent substrate (Biorad).

592 Primary antibodies used: Antibody anti-Acetylated Tubulin (1:10000; clone 6-11B-1, mouse monoclonal,  
593 T-6793 Sigma Aldrich), anti- $\alpha$ TAT1 (1:400; HPA046816, rabbit, Atlas Antibodies), anti-Poly-Glu Tubulin  
594 (1:1000; AbC0101, ValBiotech), anti- $\alpha$ -Tubulin (1:1000; MCA77G, rat, Biorad), anti- $\beta_1$  integrin (ab52971,  
595 Abcam), anti-Talin (1:1000; T3287, mouse monoclonal, clone 8D4, lot 035M4805V; Sigma-Aldrich), anti-  
596 GEF-H1 (1:100; ab155785, Abcam), anti-GAPDH (MAB374, lot 2689153 Millipore). Secondary HRP  
597 antibodies were all purchased from Jackson ImmunoResearch. Unmodified western blots of Figures 1, 4  
598 and 5, as well as Extended Data Figures 1, 2 and 3 can be found in the corresponding source data files.

## 599 **Graphs and statistics**

600 All graphs and statistics were done using Graphpad Prism.

601

## 602 **Data availability**

---

603

604 The data supporting the findings of this study are available within the manuscript. The mass  
605 spectrometry proteomics data have been deposited to the ProteomeXchange Consortium via the  
606 PRIDE<sup>52,53</sup> partner repository with the dataset identifier PXD015871 (username:  
607 reviewer89842@ebi.ac.uk; password: EC4DSdRf; project name: Potential interactors of alpha-tubulin  
608 acetyltransferase 1 ( $\alpha$ TAT1/MEC17). Unmodified western blots of Figures 1, 4 and 5, as well as Extended

609 Data Figures 1, 2 and 3 can be found in the corresponding source data files. Other raw data generated  
610 during this study are available on reasonable request.

611

## 612 **Code availability**

---

613

614 Codes for focal adhesion distribution and traction forces are available from the authors upon request.

615

## 616 References

- 617 1 Jaalouk, D. E. & Lammerding, J. Mechanotransduction gone awry. *Nat Rev Mol Cell Biol* **10**, 63-  
618 73, doi:10.1038/nrm2597 (2009).
- 619 2 Sun, Z., Guo, S. S. & Fässler, R. Integrin-mediated mechanotransduction. *The Journal of Cell*  
620 *Biology* **215**, 445-456, doi:10.1083/jcb.201609037 (2016).
- 621 3 Elosegui-Artola, A. *et al.* Rigidity sensing and adaptation through regulation of integrin types.  
622 *Nat Mater* **13**, 631-637 (2014).
- 623 4 Ladoux, B., Mège, R.-M. & Trepant, X. Front-Rear Polarization by Mechanical Cues: From Single  
624 Cells to Tissues. *Trends Cell Biol.* **26**, 420-433, doi:10.1016/j.tcb.2016.02.002 (2016).
- 625 5 Etienne-Manneville, S. Microtubules in cell migration. *Annu Rev Cell Dev Biol* **29**, 471-499,  
626 doi:10.1146/annurev-cellbio-101011-155711 (2013).
- 627 6 Bouchet, B. P. & Akhmanova, A. Microtubules in 3D cell motility. *J. Cell Sci.* **130**, 39-50,  
628 doi:10.1242/jcs.189431 (2017).
- 629 7 Martins, G. G. & Kolega, J. A role for microtubules in endothelial cell protrusion in three-  
630 dimensional matrices. *Biol. Cell* **104**, 271-286 (2012).
- 631 8 Seetharaman, S. & Etienne-Manneville, S. Microtubules at focal adhesions – a double-edged  
632 sword. *J. Cell Sci.* **132**, jcs232843, doi:10.1242/jcs.232843 (2019).
- 633 9 Lyle, K. S., Corleto, J. A. & Wittmann, T. Microtubule dynamics regulation contributes to  
634 endothelial morphogenesis. *Bioarchitecture* **2**, 220-227, doi:10.4161/bioa.22335 (2012).
- 635 10 Myers, K. A., Applegate, K. T., Danuser, G., Fischer, R. S. & Waterman, C. M. Distinct ECM  
636 mechanosensing pathways regulate microtubule dynamics to control endothelial cell branching  
637 morphogenesis. *J. Cell Biol.* **192**, 321-334, doi:10.1083/jcb.201006009 (2011).
- 638 11 Etienne-Manneville, S. & Hall, A. Integrin-mediated activation of Cdc42 controls cell polarity in  
639 migrating astrocytes through PKCzeta. *Cell* **106**, 489-498 (2001).
- 640 12 Etienne-Manneville, S. In vitro assay of primary astrocyte migration as a tool to study Rho  
641 GTPase function in cell polarization. *Methods Enzymol* **406**, 565-578, doi:10.1016/S0076-  
642 6879(06)06044-7 (2006).
- 643 13 Bance, B., Seetharaman, S., Leduc, C., Boëda, B. & Etienne-Manneville, S. Microtubule  
644 acetylation but not deetyrosination promotes focal adhesion dynamics and astrocyte migration.  
645 *Journal of Cell Science* **132**, jcs.225805, doi:10.1242/jcs.225805 (2019).
- 646 14 Coombes, C. *et al.* Mechanism of microtubule lumen entry for the  $\alpha$ -tubulin acetyltransferase  
647 enzyme  $\alpha$ TAT1. *Proceedings of the National Academy of Sciences* **113**, E7176-E7184,  
648 doi:10.1073/pnas.1605397113 (2016).
- 649 15 Valenzuela-Fernandez, A., Cabrero, J. R., Serrador, J. M. & Sánchez-Madrid, F. HDAC6: a key  
650 regulator of cytoskeleton, cell migration and cell–cell interactions. *Trends Cell Biol.* **18**, 291-297  
651 (2008).
- 652 16 Haggarty, S. J., Koeller, K. M., Wong, J. C., Butcher, R. A. & Schreiber, S. L. Multidimensional  
653 Chemical Genetic Analysis of Diversity-Oriented Synthesis-Derived Deacetylase Inhibitors Using  
654 Cell-Based Assays. *Chem. Biol.* **10**, 383-396, doi:10.1016/S1074-5521(03)00095-4 (2003).
- 655 17 Haggarty, S. J., Koeller, K. M., Wong, J. C., Grozinger, C. M. & Schreiber, S. L. Domain-selective  
656 small-molecule inhibitor of histone deacetylase 6 (HDAC6)-mediated tubulin deacetylation.  
657 *Proceedings of the National Academy of Sciences* **100**, 4389-4394,  
658 doi:10.1073/pnas.0430973100 (2003).
- 659 18 De Pascalis, C. & Etienne-Manneville, S. Single and collective cell migration: the mechanics of  
660 adhesions. *Mol Biol Cell* **28**, 1833-1846, doi:10.1091/mbc.E17-03-0134 (2017).
- 661 19 Seetharaman, S. & Etienne-Manneville, S. Integrin diversity brings specificity in  
662 mechanotransduction. *Biol. Cell* **110**, 49-64, doi:10.1111/boc.201700060 (2018).

663 20 Cluzel, C. *et al.* The mechanisms and dynamics of  $\alpha\beta3$  integrin clustering in living cells. *J. Cell*  
664 *Biol.* **171**, 383-392, doi:10.1083/jcb.200503017 (2005).

665 21 Janke, C. & Montagnac, G. Causes and Consequences of Microtubule Acetylation. *Curr. Biol.* **27**,  
666 R1287-R1292 (2017).

667 22 Enomoto, T. Microtubule disruption induces the formation of actin stress fibers and focal  
668 adhesions in cultured cells: possible involvement of the rho signal cascade. *Cell Struct Funct* **21**,  
669 317-326 (1996).

670 23 Bershadsky, A., Chausovsky, A., Becker, E., Lyubimova, A. & Geiger, B. Involvement of  
671 microtubules in the control of adhesion-dependent signal transduction. *Curr. Biol.* **6**, 1279-1289,  
672 doi:[https://doi.org/10.1016/S0960-9822\(02\)70714-8](https://doi.org/10.1016/S0960-9822(02)70714-8) (1996).

673 24 Choquet, D., Felsenfeld, D. P. & Sheetz, M. P. Extracellular matrix rigidity causes strengthening of  
674 integrin-cytoskeleton linkages. *Cell* **88**, 39-48 (1997).

675 25 Wolfenson, H. *et al.* Tropomyosin controls sarcomere-like contractions for rigidity sensing and  
676 suppressing growth on soft matrices. *Nat. Cell Biol.* **18**, 33-42, doi:10.1038/ncb3277 (2016).

677 26 Peglion, F., Llense, F. & Etienne-Manneville, S. Adherens junction treadmill during collective  
678 migration. *Nat. Cell Biol.* **16**, 639 (2014).

679 27 Dupont, S. *et al.* Role of YAP/TAZ in mechanotransduction. *Nature* **474**, 179-183,  
680 doi:10.1038/nature10137 (2011).

681 28 Panciera, T., Azzolin, L., Cordenonsi, M. & Piccolo, S. Mechanobiology of YAP and TAZ in  
682 physiology and disease. *Nature Reviews Molecular Cell Biology* **18**, 758-770,  
683 doi:10.1038/nrm.2017.87 (2017).

684 29 Jansen, K. A., Atherton, P. & Ballestrem, C. Mechanotransduction at the cell-matrix interface.  
685 *Semin. Cell Dev. Biol.* **71**, 75-83, doi:<https://doi.org/10.1016/j.semcdb.2017.07.027> (2017).

686 30 Prager-Khoutorsky, M. *et al.* Fibroblast polarization is a matrix-rigidity-dependent process  
687 controlled by focal adhesion mechanosensing. *Nat. Cell Biol.* **13**, 1457, doi:10.1038/ncb2370  
688 <https://www.nature.com/articles/ncb2370#supplementary-information> (2011).

689 31 Tran, A. D.-A. *et al.* HDAC6 deacetylation of tubulin modulates dynamics of cellular adhesions.  
690 *Journal of cell science* **120**, 1469-1479 (2007).

691 32 De Pascalis, C. *et al.* Intermediate filaments control collective migration by restricting traction  
692 forces and sustaining cell-cell contacts. *J. Cell Biol.* **217**, 3031-3044, doi:10.1083/jcb.201801162  
693 (2018).

694 33 Sakamoto, Y., Boëda, B. & Etienne-Manneville, S. APC binds intermediate filaments and is  
695 required for their reorganization during cell migration. *J. Cell Biol.* **200**, 249-258 (2013).

696 34 Schiller, H. B. *et al.* beta1- and alphaV-class integrins cooperate to regulate myosin II during  
697 rigidity sensing of fibronectin-based microenvironments. *Nat. Cell Biol.* **15**, 625-636,  
698 doi:10.1038/ncb2747 (2013).

699 35 Lawson, C. D. & Ridley, A. J. Rho GTPase signaling complexes in cell migration and invasion. *J.*  
700 *Cell Biol.* **217**, 447-457, doi:10.1083/jcb.201612069 (2018).

701 36 Krendel, M., Zenke, F. T. & Bokoch, G. M. Nucleotide exchange factor GEF-H1 mediates cross-  
702 talk between microtubules and the actin cytoskeleton. *Nat Cell Biol* **4**, 294-301 (2002).

703 37 Ren, Y., Li, R., Zheng, Y. & Busch, H. Cloning and characterization of GEF-H1, a microtubule-  
704 associated guanine nucleotide exchange factor for Rac and Rho GTPases. *J Biol Chem* **273**,  
705 34954-34960 (1998).

706 38 Heck, J. N. *et al.* Microtubules regulate GEF-H1 in response to extracellular matrix stiffness. *Mol.*  
707 *Biol. Cell* **23**, 2583-2592, doi:10.1091/mbc.E11-10-0876 (2012).

708 39 Rafiq, N. B. M. *et al.* A mechano-signalling network linking microtubules, myosin IIA filaments  
709 and integrin-based adhesions. *Nature materials* **18**, 638-649, doi:10.1038/s41563-019-0371-y  
710 (2019).

711 40 Jiu, Y. *et al.* Vimentin intermediate filaments control actin stress fiber assembly through GEF-H1  
712 and RhoA. **130**, 892-902, doi:10.1242/jcs.196881 (2017).

713 41 Trepap, X. *et al.* Physical forces during collective cell migration. *Nature Physics* **5**, 426-430,  
714 doi:10.1038/nphys1269 (2009).

715 42 Legerstee, K., Geverts, B., Slotman, J. A. & Houtsmuller, A. B. Dynamics and distribution of  
716 paxillin, vinculin, zyxin and VASP depend on focal adhesion location and orientation. *Scientific*  
717 *reports* **9**, 10460, doi:10.1038/s41598-019-46905-2 (2019).

718 43 Barriga, E. H., Franze, K., Charras, G. & Mayor, R. Tissue stiffening coordinates morphogenesis by  
719 triggering collective cell migration in vivo. *Nature* **554**, 523-527, doi:10.1038/nature25742  
720 (2018).

721 44 Leal-Egaña, A. *et al.* The size-speed-force relationship governs migratory cell response to  
722 tumorigenic factors. *Mol. Biol. Cell* **28**, 1612-1621, doi:10.1091/mbc.E16-10-0694 (2017).

723 45 Sunyer, R. *et al.* Collective cell durotaxis emerges from long-range intercellular force  
724 transmission. *Science* **353**, 1157-1161, doi:10.1126/science.aaf7119 (2016).

725 46 Serra-Picamal, X., Conte, V., Sunyer, R., Muñoz, J. J. & Trepap, X. in *Methods Cell Biol.* Vol. 125  
726 309-330 (Elsevier, 2015).

727 47 Tambe, D. T. *et al.* Collective cell guidance by cooperative intercellular forces. *Nat. Mater.* **10**,  
728 469 (2011).

729 48 Heuser, J. The production of 'cell cortices' for light and electron microscopy. *Traffic* **1**, 545-552,  
730 doi:10.1034/j.1600-0854.2000.010704.x (2000).

731 49 Martiel, J. L. *et al.* Measurement of cell traction forces with ImageJ. *Methods Cell Biol* **125**, 269-  
732 287, doi:10.1016/bs.mcb.2014.10.008 (2015).

733 50 Pouillet, P., Carpentier, S. & Barillot, E. myProMS, a web server for management and validation  
734 of mass spectrometry-based proteomic data. *Proteomics* **7**, 2553-2556,  
735 doi:10.1002/pmic.200600784 (2007).

736 51 Valot, B., Langella, O., Nano, E. & Zivy, M. MassChroQ: a versatile tool for mass spectrometry  
737 quantification. *Proteomics* **11**, 3572-3577, doi:10.1002/pmic.201100120 (2011).

738 52 Vizcaino, J. A. *et al.* 2016 update of the PRIDE database and its related tools. *Nucleic Acids Res*  
739 **44**, D447-456, doi:10.1093/nar/gkv1145 (2016).

740 53 Perez-Riverol, Y. *et al.* The PRIDE database and related tools and resources in 2019: improving  
741 support for quantification data. *Nucleic Acids Res.* **47**, D442-d450, doi:10.1093/nar/gky1106  
742 (2019).

743

744

745

746

747

748

749

750

751

752

## 753 **Acknowledgements**

---

754

755 This work was supported by the La Ligue contre le cancer (S-CR17017), Centre National de la Recherche  
756 Scientifique and Institut Pasteur. SS is funded by the ITN PolarNet Marie Curie grant and Fondation pour  
757 la Recherche Médicale (FDT201904007930) and was enrolled at the Ecole Doctorale FIRE Frontières de  
758 l'Innovation en Recherche et Éducation (Frontières du Vivant FdV – Programme Bettencourt), CRI and  
759 the Université de Paris. We would like to thank Anna Akhmanova for providing GFP-Talin construct,  
760 Cécile Leduc for FA distribution macro, Bertille Bance and Franck Coumilleau for discussions, Nisha  
761 Mohd Rafiq for fixation protocols and discussions, Emma van Bodegraven for critical reading of the  
762 manuscript and discussions.

## 763 **Author contributions**

---

764

765 S.S. designed, performed experiments, analysed and interpreted the results, and wrote the paper; B.V.  
766 assisted in the setup of TFM experiments and analysis, helped with data interpretation and discussions;  
767 V.R. performed immunoprecipitation and pull down experiments; A. F. carried out a part of the  
768 experiments using HUVECs; C. D-P helped with experimental techniques and discussions; B. B optimised  
769 the GFP-nanobody and IP conditions used for mass spectrometry sample preparation and set up the  
770 chemical wound assay; F. D. carried out the MS experimental work; D. L. supervised the MS experiments  
771 and data analysis; S.V. performed EM experiments; A. B. helped with data interpretation and  
772 discussions; M.T. provided ideas, helped with data interpretation and discussions; S. E-M. supervised the  
773 project, interpreted the results, and wrote the paper.

## 774 **Competing interests**

---

775

776 Authors declare no competing interests.

777



## 778 Main figure legends

779

780 **Figure 1: Integrin-mediated signalling and substrate rigidity regulate microtubule acetylation. a, b, c.**  
781 Astrocytes (WT) or treated with **c (i, ii)**. Ctl, Src kin 1 or PF-562271, plated on PAA gels; **(a. i, c. i)** images  
782 showing Acetylated tubulin and  $\alpha$ -tubulin; **(b. i, b. ii)** western blots showing normalised ratio of  
783 acetylated tubulin over GAPDH. **(a)** n = 77 for 1.26 kPa, 88 for 2 kPa, 67 for 9 kPa and 81 for 48 kPa; **(c)** n  
784 = 30 for Ctl, 43 for Src kin1, 43 for PF-562271. **d, e.** Astrocyte lysate pulldown (PD; WT cells) and  
785 immunoprecipitations (cells transfected with GFP-Ctl or GFP- $\alpha$ TAT1), using (d) GST- $\alpha$ TAT1 and (e) GFP-  
786  $\alpha$ TAT1 resin respectively. Westerns showing Talin and Acetylated tubulin. **f.** Images of GFP- $\alpha$ TAT1 and  
787 mCherry-vinculin astrocytes transfected along with siCtl or siTalin1. **g.** Astrocytes on 48 kPa PAA gels  
788 showing **(g. i)** Acetylated tubulin and  $\alpha$ -tubulin; **(g. ii)** ratio of the intensities of Acetylated tubulin over  
789 total Tubulin intensity; n = 51 for siCtl and 56 for siTalin1. **h.** Pulldown (PD; Ctl or Y-27632 treated cells)  
790 using GST- $\alpha$ TAT1 resin; **(h. i)** Westerns showing Talin and Ponceau staining; **(h. ii)** normalised Talin in  
791 DMSO (Ctl) and Y-27632 treated cells. **i.** Images showing GFP- $\alpha$ TAT1 and mCherry-vinculin expressing  
792 astrocytes treated with DMSO (Ctl) or Y-27632. **j, k.** Migrating astrocytes, treated with DMSO (Ctl) or  
793 ROCK inhibitor Y-27632 for 2 h; **(j)** Western blot showing the levels of Acetylated tubulin and GAPDH in  
794 Ctl or Y-27632 treated cells; **(k. i, ii)** ratio of the intensities of Acetylated tubulin over total Tubulin  
795 intensity; n = 98 for Ctl, 79 for Y-27632 treated cells respectively. **Scale bar** (a, c, g): 10  $\mu$ m, (f, k): 20  $\mu$ m.  
796 **Number of independent experiments** = 4 (for a, h), 5 (for b, i), 2 (for c), 3 (for d-g, j, k). In box-and-  
797 whisker plots, box extends from the 25<sup>th</sup> to 75<sup>th</sup> percentile, whiskers show minimum and maximum  
798 values, and the line within the box represents the median. **Statistical tests:** One-way ANOVA followed by  
799 Tukey's multiple comparison's test (for a, b, g), Paired t-test (for h), Unpaired Student's t-test (two-  
800 tailed; for k).

801

802 **Figure 2: Microtubule acetylation tunes cell mechanosensitivity.** **a, b.** Astrocytes transfected with siCtl  
803 and si $\alpha$ TAT1-2, or treated with Niltubacin and Tubacin, or **c.** HUVECs treated with Niltubacin and  
804 Tubacin plated on PAA gels of different rigidities; **(a-c. i)** stained for YAP and  $\alpha$ -tubulin (not shown) to  
805 mark the cell boundary (marked by dotted lines); **(a-c. ii)** ratio of the YAP intensity in the nucleus over  
806 cytoplasm; (a) n = 49 for 2 kPa siCtl, 44 for 2 kPa si $\alpha$ TAT1-2, 68 for 48 kPa siCtl, 74 for 48 kPa si $\alpha$ TAT1-2;  
807 (b) n = 49 for 2 kPa Niltubacin, 53 for 2 kPa Tubacin, 51 for 48 kPa Niltubacin and 51 for 48 kPa Tubacin;  
808 (c) n = 26 for 2 kPa Niltubacin, 25 for 2 kPa Tubacin, 32 for 48 kPa Niltubacin and 26 for 48 kPa Tubacin.  
809 **d.** Astrocytes (WT) plated on PAA gels of different rigidities, **(d. i)** stained for  $\alpha$ -tubulin and Talin. Images  
810 shown correspond to the same cells depicted in Fig. 1A; **(d. ii)** FA density in different regions of the cells;  
811 n = 40 for 1.26 kPa, 51 for 2 kPa, 94 for 9 kPa, 77 for 48 kPa. **e, f.** Astrocytes transfected with siCtl and  
812 si $\alpha$ TAT1-2, or treated with Niltubacin and Tubacin, plated on PAA gels of different substrate rigidities,  
813 and **(e. i, f. i)** stained for Paxillin; **(e. ii, f. ii)** FA density (number of FAs/ $\mu\text{m}^2$ ) in the central region (16  $\mu\text{m}$ -  
814 cell center) of cells depicted in panels e and f; n = 60 for 1.26 kPa siCtl, 36 for 1.26 kPa si $\alpha$ TAT1-2, 54 for  
815 48 kPa siCtl and 47 for 48 kPa si $\alpha$ TAT1-2; n = 59 for 1.26 kPa Niltubacin, 55 for 1.26 kPa Tubacin, 46 for  
816 48 kPa Niltubacin and 37 for 48 kPa Tubacin. **g.** Schematic (summarising a-f) showing focal adhesion  
817 distribution upon manipulation of microtubule acetylation. **Scale bar** (a-f): 10  $\mu\text{m}$ ; **Number of**  
818 **independent experiments** = 3 (for a, b, d-f), 2 (for c); In box-and-whisker plots, box extends from the  
819 25<sup>th</sup> to 75<sup>th</sup> percentile, whiskers show minimum and maximum values, and the line within the box  
820 represents the median; **Statistical tests:** one-way ANOVA followed by Tukey's multiple comparison's  
821 test (for a, b, e, f), two-way ANOVA followed by Tukey's multiple comparison's test (for d).

822

823 **Figure 3: Microtubule acetylation reorganises the actomyosin and intermediate filament networks.** **a,**  
824 **b, c.** Astrocytes transfected with siCtl or si $\alpha$ TAT1, and stained for **(a. i)** Actin, pMLC and Paxillin; **(b)**  
825 Myosin IIa, Acetylated tubulin and  $\alpha$ -tubulin; **(c)** Vimentin and  $\alpha$ -tubulin; **(a. ii)** percentage of cells with

826 inter-junctional transverse arcs; n = 199 for siCtl and 159 si $\alpha$ TAT1-2. **d.** Ultrastructural organization of  
827 focal adhesion-associated cytoskeleton in siCtl or si $\alpha$ TAT1-2 depleted cells; **d (i)** Platinum replica  
828 electron microscopy (PREM) survey view of the cytoplasmic surface of the leading edge in siCtl unroofed  
829 cells. Boxed regions correspond to focal adhesions. Extracellular space is pseudo-coloured in purple. (1,  
830 2) High magnification views corresponding to the boxed regions in panel (i). White arrows indicate  
831 microtubules and yellow arrowheads denote intermediate filaments. (3) Zoom-in region corresponding  
832 to the boxed region in marked in region (2). Scale bar: 1  $\mu$ m. White arrows indicate microtubules and  
833 yellow arrowheads denote intermediate filaments. Scale bar: 2  $\mu$ m and 1  $\mu$ m. **d (ii, iii)** PREM survey view  
834 of the cytoplasmic surface of the leading edge in  $\alpha$ TAT1-depleted cells. Extracellular space is pseudo-  
835 coloured in purple. Scale bars: 10  $\mu$ m, 1  $\mu$ m (inset). (4, 5) High magnification views corresponding to the  
836 boxed regions in panel ii and iii respectively. Scale bar: 1  $\mu$ m. **e.** HUVECs treated with DMSO or Tubacin,  
837 stained for Actin, Vinculin and Myosin IIA. **f.** Astrocytes treated with Niltubacin or Tubacin, stained for  
838 Actin and Paxillin. **Scale bar** (a-c): 20  $\mu$ m, (e, f): 10  $\mu$ m. In box-and-whisker plots, box extends from the  
839 25<sup>th</sup> to 75<sup>th</sup> percentile, whiskers show minimum and maximum values, and the line within the box  
840 represents the median. **Number of independent experiments** = 3 (for a-c); **Statistical tests:** Paired  
841 Student's t-test (two-tailed; for a).

842

843 **Figure 4: Microtubule acetylation promotes traction force generation and Rho activation. a, b, c, d. (a-**  
844 **d. i)** Stress-field maps of astrocytes on crossbow-shaped micropatterned PAA gels of different rigidities,  
845 transfected with (a) siCtl and si $\alpha$ TAT1-2, (b) siCtl + GFP- $\alpha$ TAT1 and si $\alpha$ TAT1-2 + GFP- $\alpha$ TAT1, or treated  
846 with (c) Niltubacin and Tubacin; or (d) HUVECs treated with Niltubacin and Tubacin; **(a, b, c. ii, d. ii)**  
847 corresponding stored energies (in Joules, J; within the range of 0 and  $5 \times 10^{-13}$  J) of cells in the above  
848 mentioned conditions; (a) n = 163 for siCtl and 141 for si $\alpha$ TAT1-2, (b) n = 74 for siCtl + GFP- $\alpha$ TAT1, and  
849 70 for si $\alpha$ TAT1-2 + GFP- $\alpha$ TAT1, (c) n = 136 for Niltubacin and 141 for Tubacin, (d) n = 83 for Niltubacin

850 and 82 for Tubacin. **e.** GST-Rhotekin pulldowns were performed using siCtl or si $\alpha$ TAT1-transfected  
851 astrocytes. Western blots showing Red Ponceau and immunoblotted for RhoA. **Scale bar** (a-d): 10  $\mu$ m;  
852 **Number of independent experiments** = 3 (for a-e). In box-and-whisker plots, the box extends from the  
853 25<sup>th</sup> to the 75<sup>th</sup> percentile, the whiskers show the minimum and maximum values, and the line within  
854 the box represents the median. **Statistical tests:** one-way ANOVA followed by Tukey's multiple  
855 comparison's test (for a, b), unpaired Student's t-test (two-tailed; for c, d).

856

857 **Figure 5: Microtubule acetylation promotes the release of GEF-H1 into the cytosol.** **a.** Migrating  
858 astrocytes transfected with siCtl, si $\alpha$ TAT1-2, and si $\alpha$ TAT1-2 followed by treatment with Tubacin, **(a. i)**  
859 stained for Acetylated tubulin,  $\alpha$ -tubulin and GEF-H1; **(a. ii)** percentage of GEF-H1 colocalised with  
860 microtubules; n = 99 for siCtl, 89 for si $\alpha$ TAT1-2, 72 for si $\alpha$ TAT1-2 + Tubacin; **b.** HUVECs treated with  
861 DMSO Ctl or Tubacin, **(b. i)** stained for  $\alpha$ -tubulin and GEF-H1; **(b. ii)** percentage of GEF-H1 colocalised  
862 with microtubules; n = 78 for DMSO Ctl and 84 for Tubacin. **c.** Immunoprecipitations using anti-GFP  
863 nanobodies were performed with lysates from HEK293 cells transfected with GFP-Ctl or GFP-GEF-H1,  
864 and treated with Nocodazole or Tubacin. Samples were analysed by immunoblotting using  $\alpha$ -tubulin,  
865 Acetylated tubulin, GEF-H1, GAPDH and GFP antibodies. **d.** Astrocytes transfected with siCtl and  
866 si $\alpha$ TAT1-2, and plated on 48 kPa PAA gels, **(d. i)** stained for GEF-H1 and  $\alpha$ -tubulin; **(d. ii)** percentage of  
867 GEF-H1 colocalised with microtubules; n = 100 for 48 kPa siCtl, 112 for 48 kPa si $\alpha$ TAT1-2, 97 for 2 kPa  
868 siCtl, 86 for 2 kPa  $\alpha$ TAT1-2 (1-2 regions per cell). **Scale bar** (a): 20  $\mu$ m, (b, d): 10  $\mu$ m. In box-and-whisker  
869 plots, the box extends from the 25<sup>th</sup> to the 75<sup>th</sup> percentile, the whiskers show the minimum and  
870 maximum values, and the line within the box represents the median. **Number of independent**  
871 **experiments** = 3 (for a-d); **Statistical tests:** Ordinary one-way ANOVA followed by Tukey's multiple  
872 comparison's test (for a, d); Unpaired Student's t-test followed by Mann-Whitney test (for b).

873 **Figure 6: Microtubule acetylation is required for mechanosensitive migration.** **a, b, c.** Phase contrast  
874 images of **(a, b. i)** Astrocytes (WT) or **(c. i)** transfected with siCtl or si $\alpha$ TAT1 migrating in a chemical  
875 wound assay on PAA gels of different rigidities for 24 h (pink and orange dotted lines show initial and  
876 final wound edge); **(b. ii, c. ii)** migration speed (in  $\mu\text{m}/\text{min}$ ) of cells at the wound edge;  $n = 123$  for 2 kPa  
877 WT, 117 for 9 kPa WT, 115 for 48 kPa WT, 91 for 2 kPa siCtl, 95 for 2 kPa si $\alpha$ TAT1-2, 93 for 48 kPa siCtl,  
878 93 for 48 kPa si $\alpha$ TAT1-2. **Scale bar** (a): 200  $\mu\text{m}$ , (b, c): 100  $\mu\text{m}$ . **Number of independent experiments = 3**  
879 (for b, c); **Statistical tests:** one-way ANOVA followed by Tukey's multiple comparison's test. In box-and-  
880 whisker plots, the box extends from the 25<sup>th</sup> to the 75<sup>th</sup> percentile, the whiskers show the minimum and  
881 maximum values, and the line within the box represents the median. **d. Proposed working model:** Cells  
882 sensing a soft substrate (d. i), with altered integrin-signalling (d. ii) exhibit less MT acetylation (d. iii). This  
883 results in GEF-H1 being bound to MTs (d. iv) and is therefore, unable to activate RhoA (d. v), which  
884 renders the cell less contractile (d. vi). In such conditions, cells generate a low amount of traction forces  
885 (d. vii) and migrate slower (d. viii). On the other hand, on stiff substrates, integrin- and talin-mediated  
886 rigidity sensing (d. i) promotes the tension-dependent recruitment of  $\alpha$ TAT1 to FAs (d. ii) and increased  
887 microtubule acetylation (d. iii). How  $\alpha$ TAT1 enters the lumen of microtubules still remains unclear  
888 although one can speculate that the recruitment of  $\alpha$ TAT1 at FAs increases the local cytosolic pool of the  
889 protein which can then enter microtubules through microtubule lattice defects or through the open  
890 ends of microtubules in close proximity to FAs ([Extended Data Fig. 5C](#)). Microtubule acetylation triggers  
891 the release of GEF-H1 from MTs (d. iv), which activates the RhoA-ROCK-myosin II pathway (d. v) to  
892 promote actomyosin contractility (d. vi), traction forces (d. vii) and cell migration (d. viii). Active GEF-H1,  
893 RhoA and ROCK are depicted in bold.

894

895

## 896 **Extended data figure legends**

---

897 **Extended Data Figure 1: a, b. (a. i)** Schematic and **(a. ii, b. i)** western blots showing **(a)** acetylation and  
898 **(b)**  $\alpha$ TAT1 levels using two distinct sets of siRNAs targeting  $\alpha$ TAT1 (si $\alpha$ TAT1-1 and si $\alpha$ TAT1-2), and  
899 Tubacin (an inhibitor of HDAC6 (deacetylase)); **(a. iii, a. iv)** ratio of the acetylated tubulin or **(b. ii)**  $\alpha$ TAT1  
900 intensity over GAPDH intensity, normalised to the values observed for the respective controls. **c.**  
901 Migrating astrocytes transfected with siCtl, **(c. i)** si $\alpha$ TAT1-1 and **(c. ii)** si $\alpha$ TAT1-2, or treated with Tubacin  
902 prior to wounding, showing acetylated tubulin and  $\alpha$ -tubulin. **d.** Astrocytes plated on PAA gels of  
903 different rigidities and treated with Tubacin; ratio of the intensities of Acetylated tubulin over total  
904 Tubulin of each cell; n = 49 for 1.26 kPa WT, 51 for 1.26 kPa Tubacin, 72 for 48 kPa WT, 66 for 48 kPa  
905 Tubacin. **e.** siCtl or WT astrocytes plated on crossbow-shaped micropatterned hydrogels of different  
906 rigidities, **(e. i)** showing Acetylated tubulin and  $\alpha$ -tubulin; **(e. ii)** ratio of the intensities of Acetylated  
907 tubulin over total Tubulin of each cell; n = 86 for 2 kPa and 103 for 48 kPa. **f.** Astrocytes plated on PAA  
908 gels of different rigidities, **(f. i)** stained with Detyrosinated tubulin and  $\alpha$ -tubulin; **(f. ii)** ratio of  
909 Detyrosinated tubulin over total tubulin intensities in each cell; n = 39 for 2 kPa, 31 for 9 kPa and 40 for  
910 48 kPa. **g. (g. i)** Western blots showing the levels of Detyrosinated tubulin and GAPDH in astrocytes  
911 plated on PAA gels of different substrate rigidities; **(g. ii)** ratio of the intensities of Detyrosinated tubulin  
912 over GAPDH normalised to the values observed for 2 kPa. **Scale bar** (c, e, f): 10  $\mu$ m; **Number of**  
913 **independent experiments** = 4 (for a - si $\alpha$ TAT1), 6 (for a - Tubacin, c, g), 3 (for b), 5 (for e), 2 (for f). In  
914 box-and-whisker plots, box extends from the 25<sup>th</sup> to 75<sup>th</sup> percentile, whiskers show minimum and  
915 maximum values, and the line within the box represents the median; **Statistical tests:** one-way ANOVA  
916 followed by Tukey's multiple comparison's test or Holm-Šidák's multiple comparisons test (a - si $\alpha$ TAT1,  
917 b, d, e, g) or Paired Student's t-test (for a - Tubacin).

918 **Extended Data Figure 2: a, b.** Astrocytes were treated with (a) RGD control or RGD peptides, (b) solvent  
919 (Ctl) or  $MnCl_2$ , and **(a. i, b. i)** stained for acetylated tubulin,  $\alpha$ -tubulin, paxillin or DAPI; **(a. ii, b. ii)** ratio of  
920 the intensities of Acetylated tubulin over total Tubulin; n = 146 for RGD control, 99 for RGD peptide, 116  
921 for Ctl and 105 for  $MnCl_2$ . **c, d.** Astrocytes were transfected with siCtl or si $\beta_1$  integrin; **(c. i)** Western blots  
922 showing levels of  $\beta_1$  integrin, Acetylated tubulin and GAPDH; **(c. ii, iii)** ratio of intensities of  $\beta_1$  integrin or  
923 Acetylated tubulin over GAPDH, normalised to the levels in siCtl respectively; **(d. i)** stained for  
924 Acetylated tubulin,  $\alpha$ -tubulin and DAPI; **(d. ii)** ratio of the intensities of Acetylated tubulin over total  
925 Tubulin; n = 122 for siCtl and 117 for si $\beta_1$  integrin. **e.** Astrocytes were treated with Ctl, Src kin 1 or PF-  
926 562271; **(e. i)** stained for Acetylated tubulin,  $\alpha$ -tubulin and Paxillin; **(e. ii)** ratio of the intensities of  
927 Acetylated tubulin over total Tubulin intensity; n = 78 for Ctl, 70 for Src kin 1, 79 for PF-562271. **f.**  
928 Astrocytes were plated on 48 kPa gels and treated with Ctl or Src kin 1. **(f. i)** Western blots showing the  
929 levels of Acetylated tubulin and GAPDH; **(f. ii)** ratio of the intensities of Acetylated tubulin over GAPDH  
930 normalised to the Ctl. **g.** Volcano plot analysis showing fold changes (GFP- $\alpha$ TAT1/GFP-Ctl) of the  
931 quantified proteins with threshold of >3 peptides, minimum absolute fold change of 1.5 (green lines)  
932 and maximum adjusted p-value of 0.05 (red line). Enriched protein interactors related to GO:0005925  
933 focal adhesion (red boxes; ratio = 1.98 and p =  $7.89 \times 10^{-5}$ ). External plots show proteins with peptides  
934 identified only in one sample type (left in GFP-Ctl and right in GFP- $\alpha$ TAT1). **h, i.** Normalised Talin  
935 interaction in (h) GST-pulldown and (i) GFP-immunoprecipitations. **j.** Western blots **(j. i)** showing the  
936 levels of Talin and GAPDH in astrocytes transfected with siCtl and siTalin; **(j. ii)** ratio of the intensities of  
937 Talin over GAPDH normalised to the Ctl. **k, l.** Astrocytes showing **(k)** GFP- $\alpha$ TAT1 localisation by  
938 epifluorescence, on microtubules, **(l)** by TIRF, at FAs, in cells treated with or without nocodazole. **Scale**  
939 **bar** (a, b, d, e, k, l): 10  $\mu$ m; **Number of independent experiments** = 3 (for a-d, h-j), 2 (for e), 4 (for f, g), 5  
940 (for l). In box-and-whisker plots, the box extends from the 25<sup>th</sup> to the 75<sup>th</sup> percentile, whiskers show the

941 minimum and maximum values, and the line within the box represents the median; **Statistical tests:**  
942 Student's t-test (for a-j).

943

944 **Extended Data Figure 3:** **a.** HUVECs plated on different substrate rigidities and **(a. i)** stained for  
945 Acetylated tubulin (insets shown) and  $\alpha$ -Tubulin; **(a. ii)** ratio of the intensities of Acetylated tubulin over  
946 total Tubulin of each cell; n = 46 for 2 kPa WT and 70 for 48 kPa. **b.** HUVECs treated with Niltubacin (Ctl)  
947 or Tubacin, and stained for Acetylated tubulin (insets shown),  $\alpha$ -tubulin and Paxillin. **c.** Western blots  
948 showing **(c. i)** Acetylated and  $\alpha$ -tubulin levels in HUVECs treated with DMSO (Ctl) and Tubacin; **(c. ii)**  
949 ratio of intensities of Acetylated tubulin over  $\alpha$ -tubulin. **d.** Schematic representation of the different cell  
950 regions used to quantify FA density (Fig. 2D-F). **e, f.** Graphs show FA density (number of FAs/ $\mu\text{m}^2$ ) in  
951 different regions of astrocytes transfected with siCtl or si $\alpha$ TAT1-2, or treated with Niltubacin or Tubacin,  
952 and plated on 1.26 kPa or 48 kPa substrates. **g, h.** Graphs show FA density (number of FAs/ $\mu\text{m}^2$ ) in  
953 different regions of astrocytes transfected with siCtl or si $\alpha$ TAT1-1, and plated on 1.26 kPa or 48 kPa  
954 substrates. **i.** siCtl or si $\alpha$ TAT1-2-transfected astrocytes plated on crossbow-shaped micropatterned  
955 polyacrylamide gels of 40 kPa or 2 kPa, **(i. i)** stained with Paxillin and  $\alpha$ -tubulin; **(i. ii)** FA density (number  
956 of FAs/ $\mu\text{m}^2$ ) within 8-16  $\mu\text{m}$  layer of the cell, or **(i. iii)** in different regions of astrocytes transfected with  
957 siCtl or si $\alpha$ TAT1-2, and plated on 2 kPa or 40 kPa substrates. **Scale bar** (a, b, i): 10  $\mu\text{m}$ . **Number of**  
958 **independent experiments** = 2 (for a), 3 (for b, e-i). In box-and-whisker plots, the box extends from the  
959 25<sup>th</sup> to the 75<sup>th</sup> percentile, the whiskers show the minimum and maximum values, and the line within  
960 the box represents the median. **Statistical tests:** Paired Student's t-test (for c), one-way ANOVA  
961 followed by Tukey's multiple comparisons test (for e-i).

962



963 **Extended Data Figure 4: a.** Astrocytes transfected with siCtl or si $\alpha$ TAT1-1, and **(a. i)** stained for Actin,  
964 Paxillin and Myosin IIa; **(a. ii)** percentage of siCtl or si $\alpha$ TAT1-transfected astrocytes with transverse  
965 interjunctional actin arcs; n = 191 for siCtl and 125 for si $\alpha$ TAT1-1; **Scale bar:** 10  $\mu$ m. **Number of**  
966 **independent experiments** = 3; **Statistical test:** Paired Student's t-test (two-tailed).

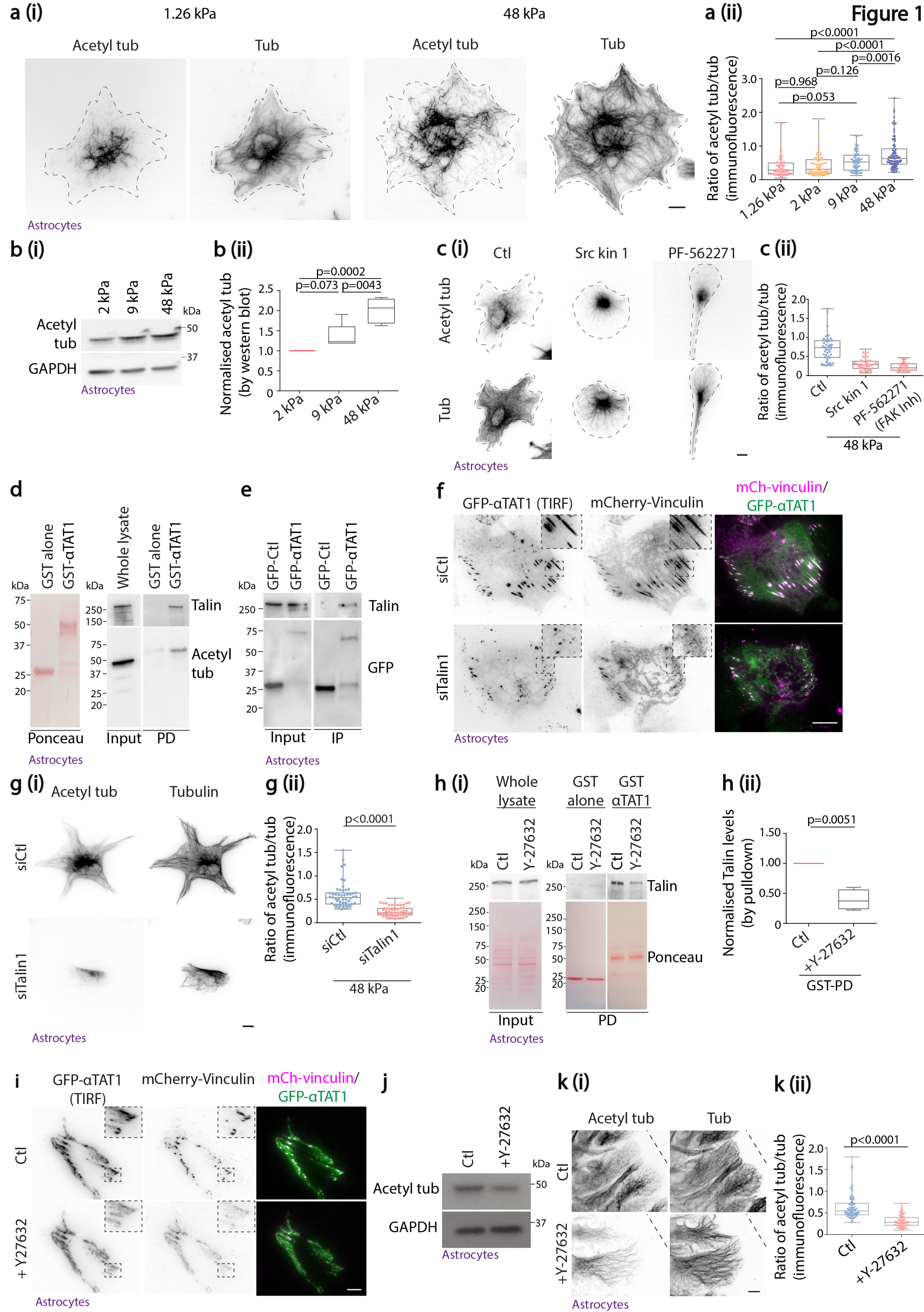
967 **Extended Data Figure 5: a.** Migrating astrocytes transfected with siCtl, si $\alpha$ TAT1-1 and si $\alpha$ TAT1-1  
968 treated with Tubacin, **(a. i)** stained for Acetylated tubulin,  $\alpha$ -tubulin and GEF-H1; **(a. ii)** percentage of  
969 GEF-H1 colocalised with microtubules; n = 119 for siCtl, 131 for si $\alpha$ TAT1-1, 103 for si $\alpha$ TAT1-1 +  
970 Tubacin. **b.** Astrocytes transfected with siCtl and si $\alpha$ TAT1-2, and plated on 2 kPa PAA gels, stained for  
971 GEF-H1 and  $\alpha$ -tubulin. **c.** Ultrastructural organization of a focal adhesion at the leading edge of a  
972 control astrocyte. Platinum replica electron microscopy (PREM) high magnification view of a focal  
973 adhesion on the cytoplasmic surface of the leading edge in siCtl unroofed astrocytes. Microtubules are  
974 both coloured in purple and indicated by white arrowheads. **d.** Traction forces in astrocytes plated on  
975 micropatterned polyacrylamide gels of different rigidities; traction forces for cells on different  
976 rigidities; Values for 2 kPa and 48 kPa are from experiments shown in Fig. 4a and 4b, pooled along with  
977 the values for 50 kPa, 91.8 kPa and 121 kPa; n = 136 for 2 kPa Niltubacin, 163 for 48 kPa siCtl, 31 for 50  
978 kPa WT, 33 for 91.8 kPa WT and 30 for 121 kPa WT. In box-and-whisker plots, the box extends from  
979 the 25<sup>th</sup> to the 75<sup>th</sup> percentile, the whiskers show the minimum and maximum values, and the line  
980 within the box represents the median. **Scale bar** (a, b): 10  $\mu$ m, (c): 200 nm; **Number of independent**  
981 **experiments** = 3 (for a, b, d - 2 kPa Niltubacin and 48 kPa siCtl), 2 (for d - 50 kPa, 91.8 kPa and 121 kPa).  
982 **Statistical tests:** One-way ANOVA followed by Tukey's multiple comparison's test (for a).

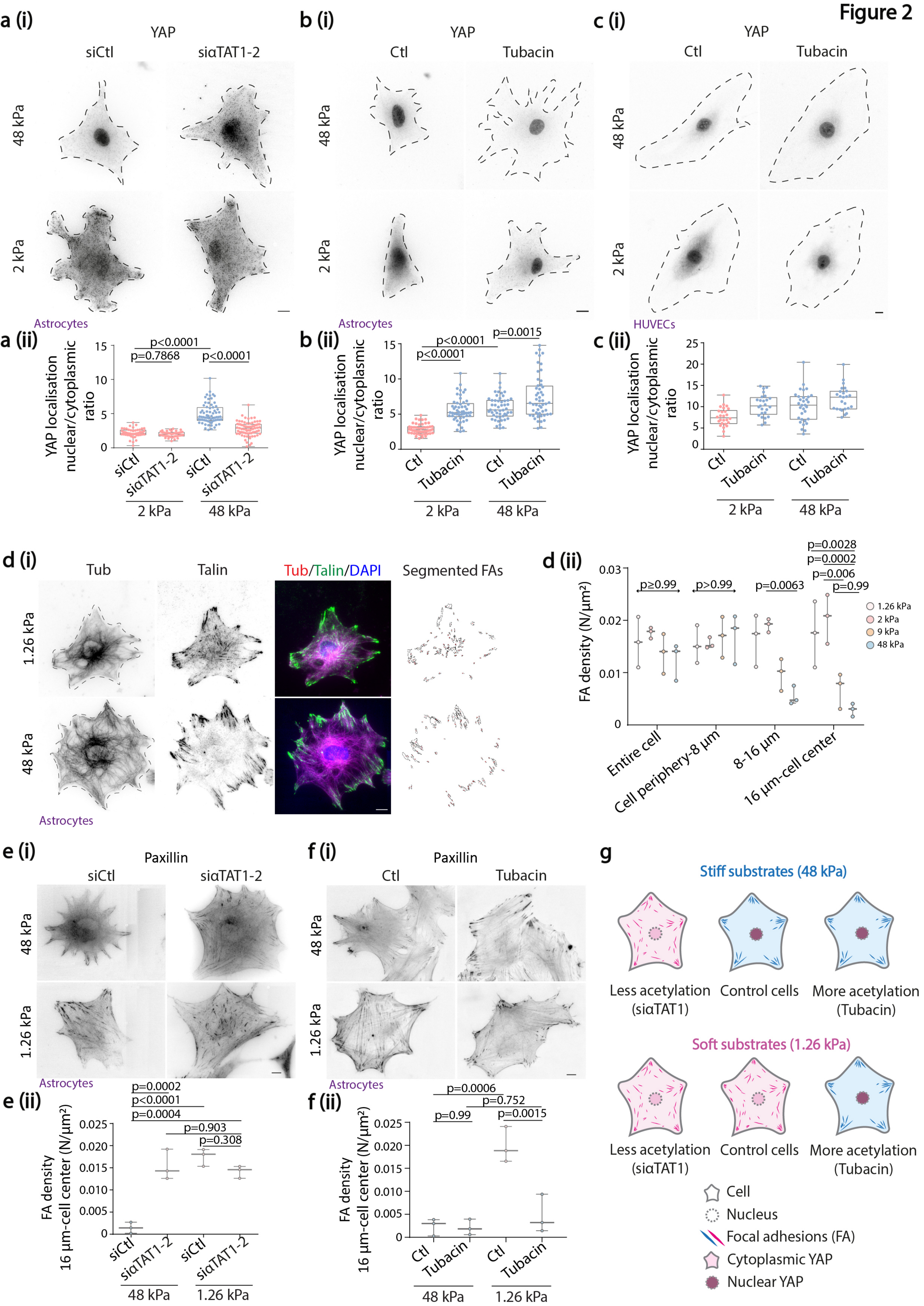
983

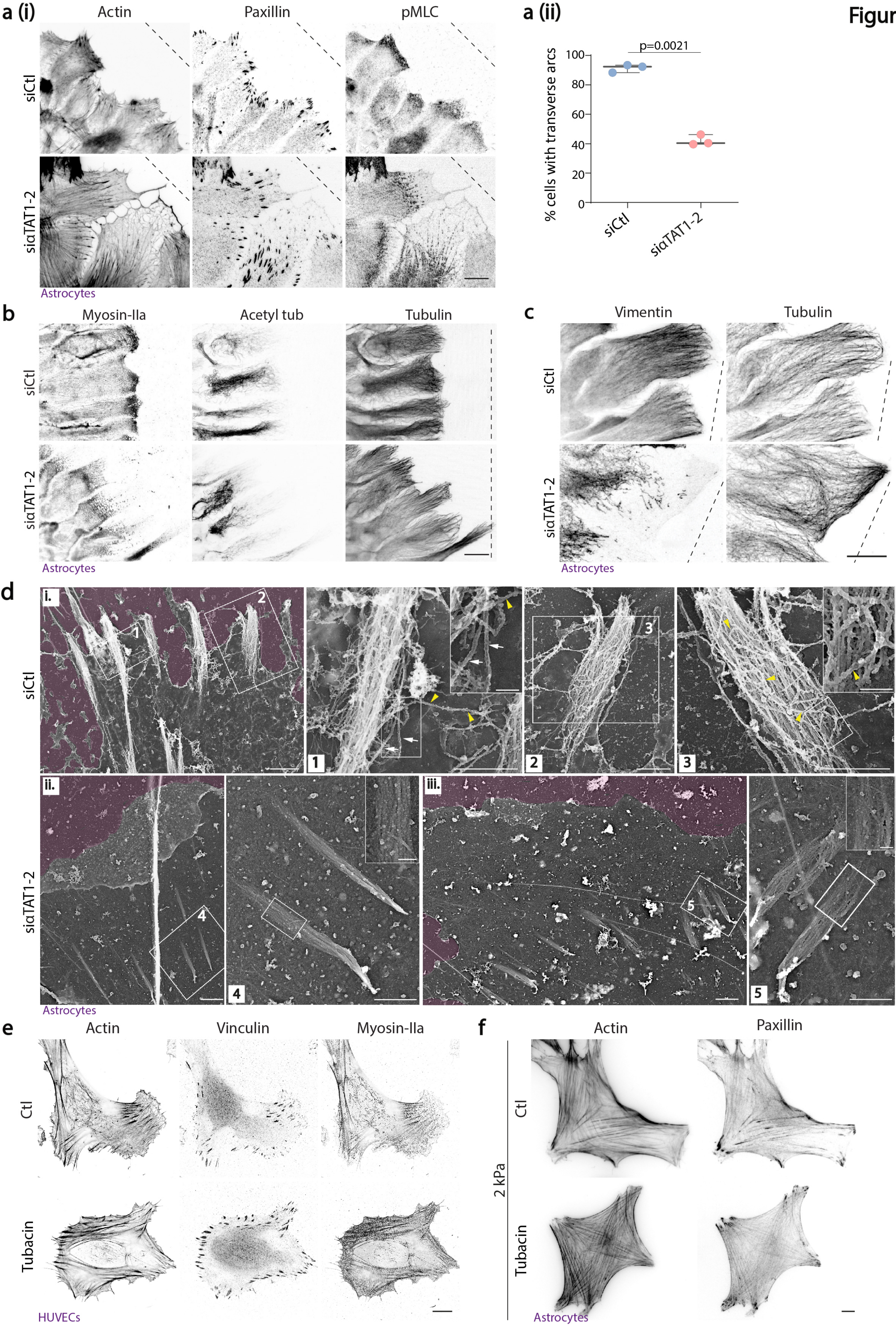
984

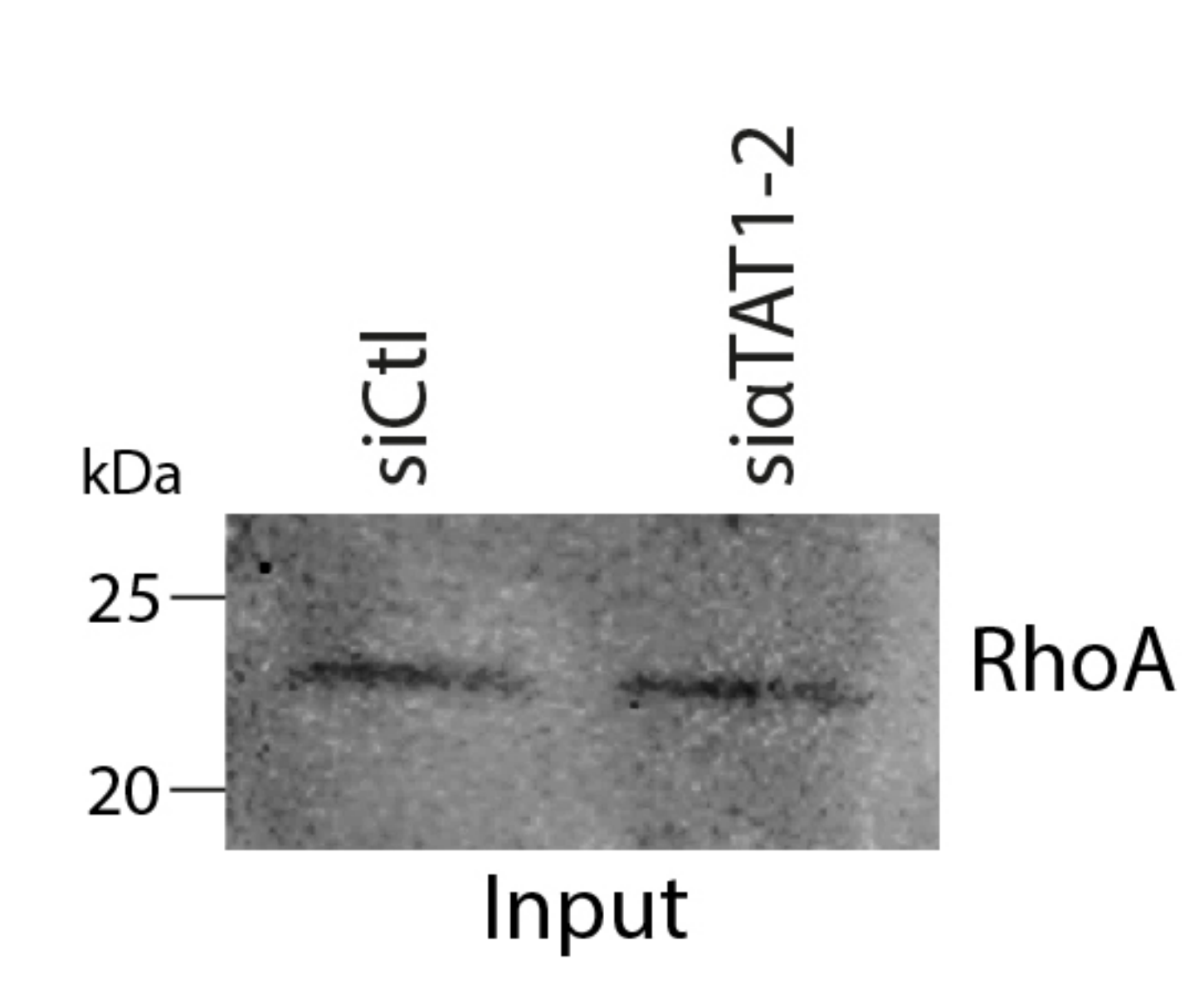
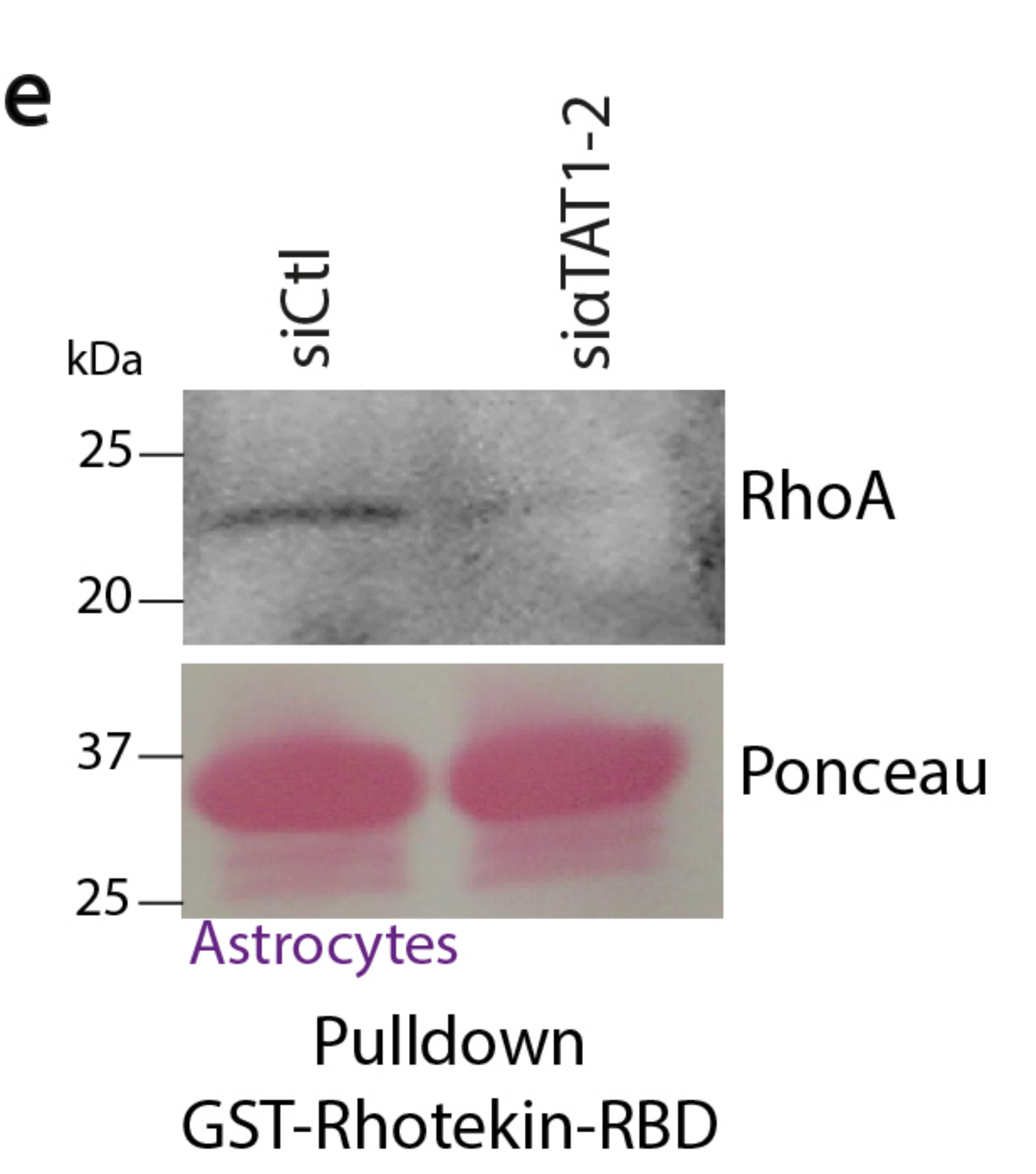
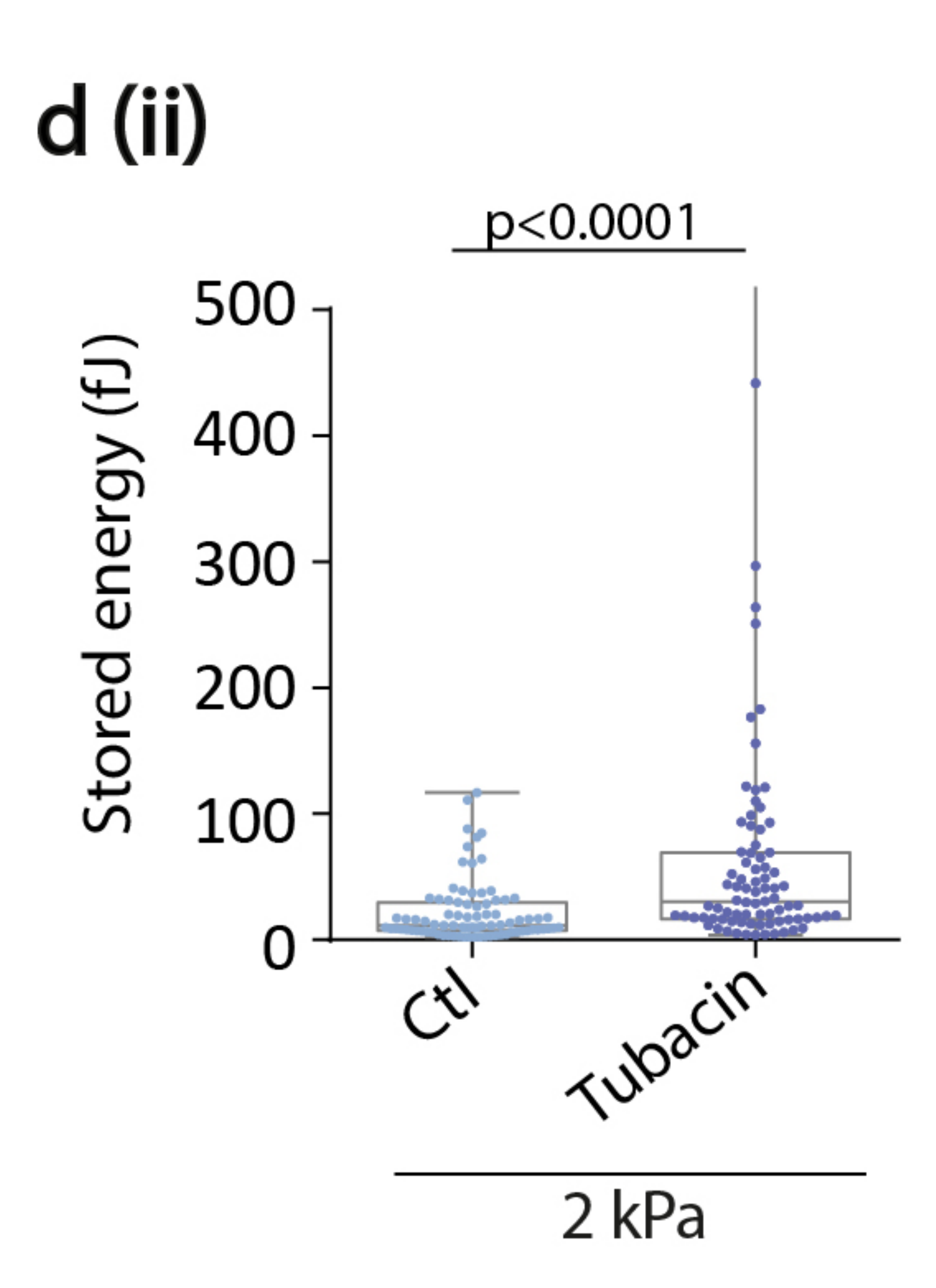
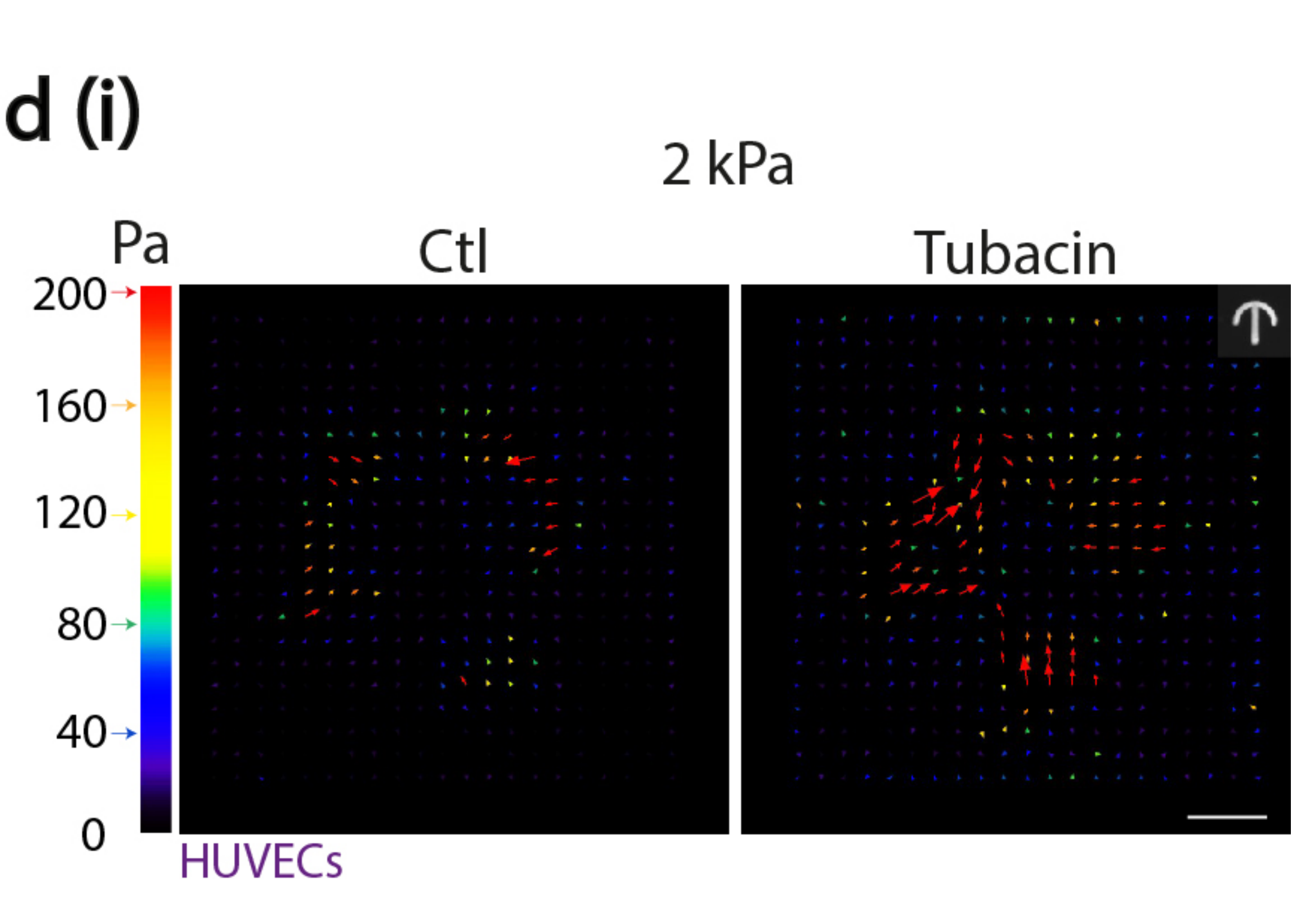
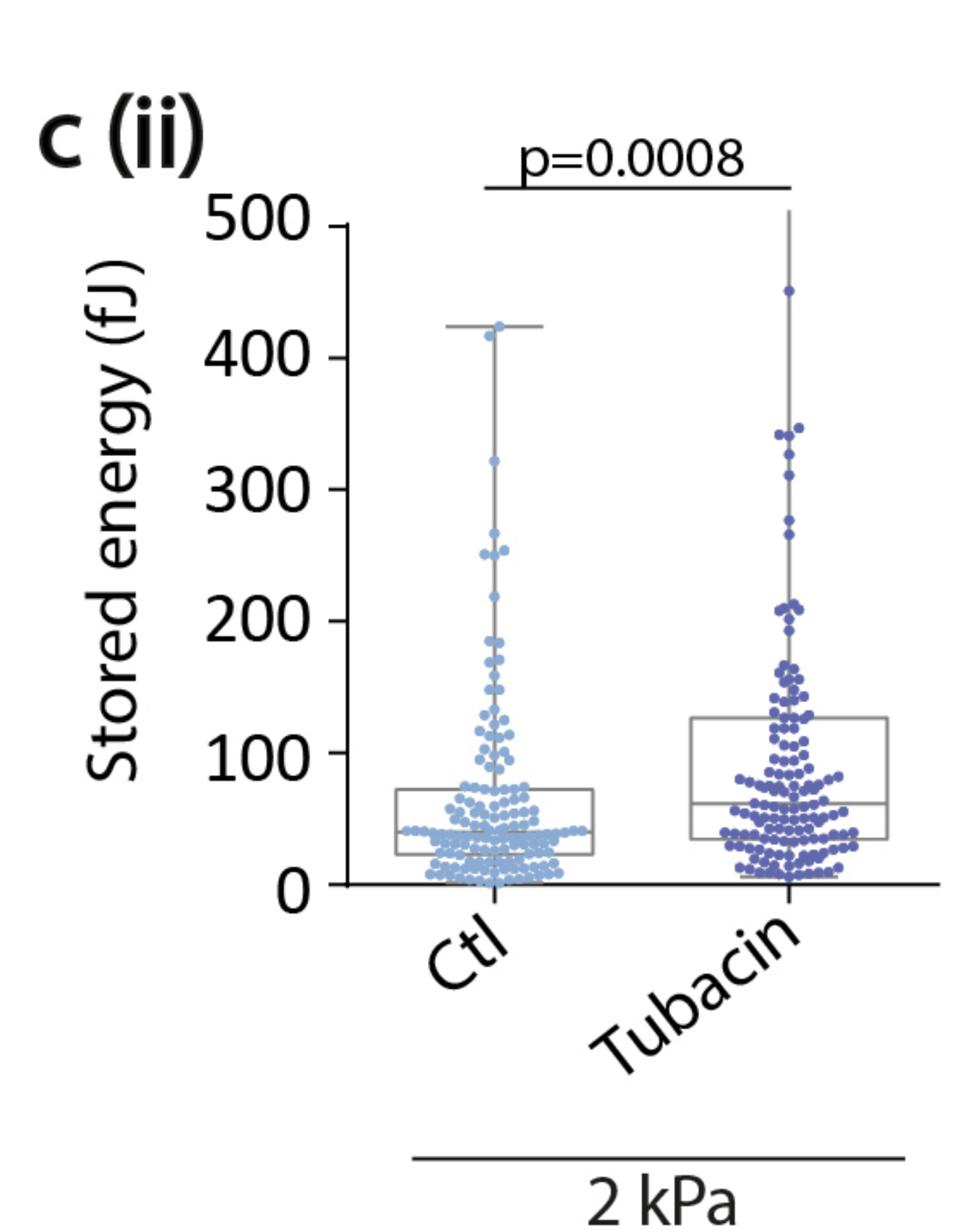
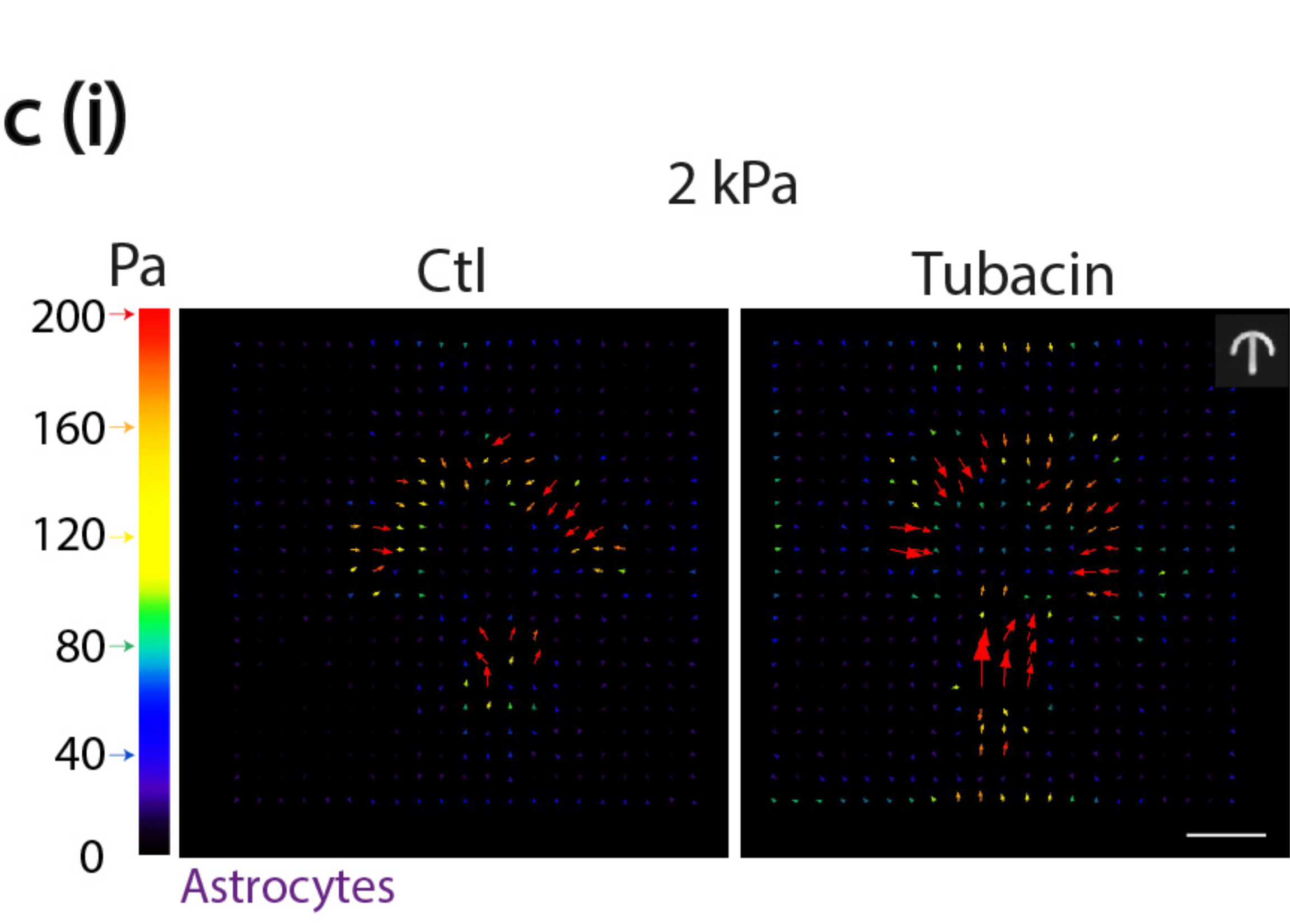
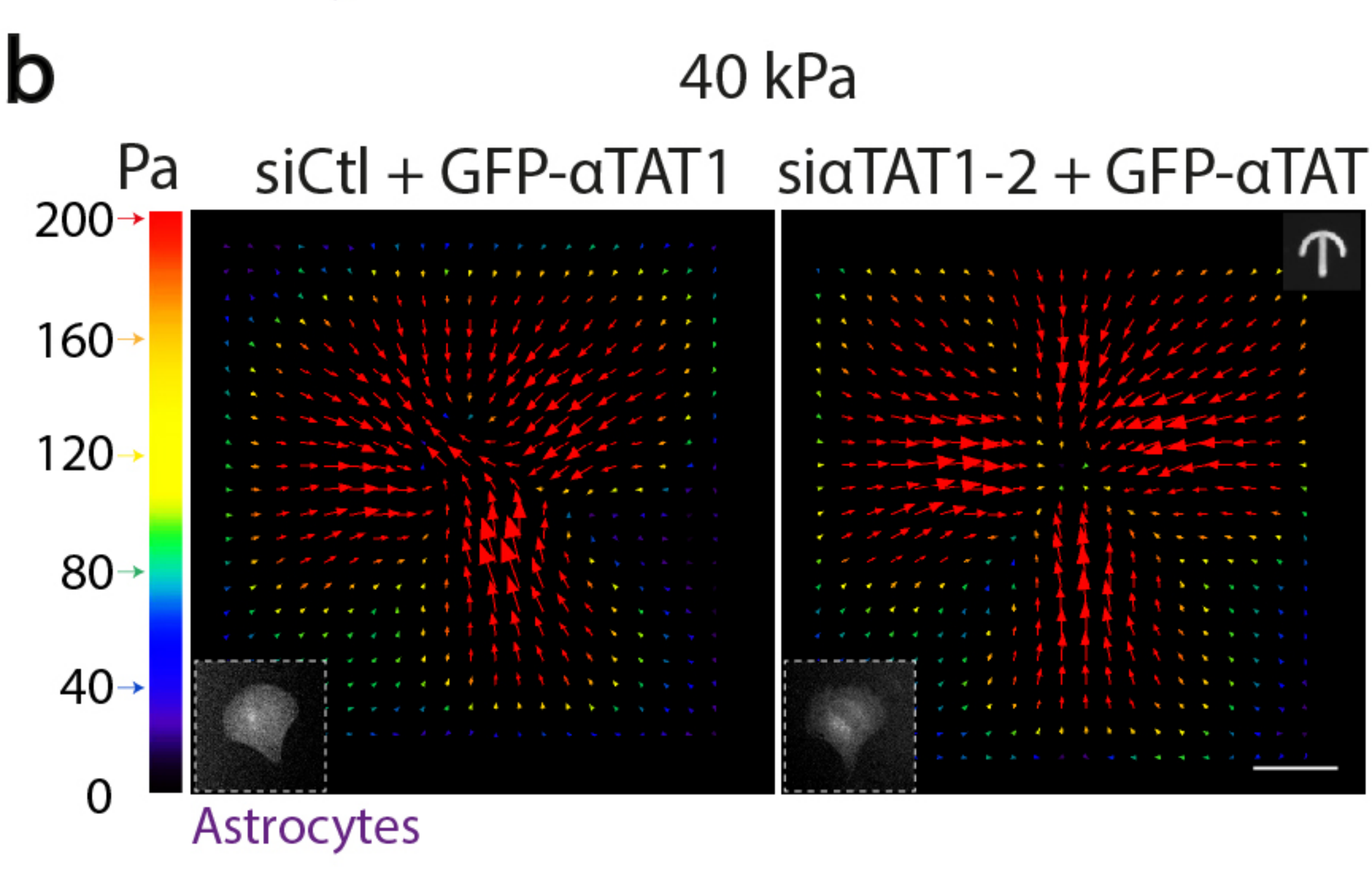
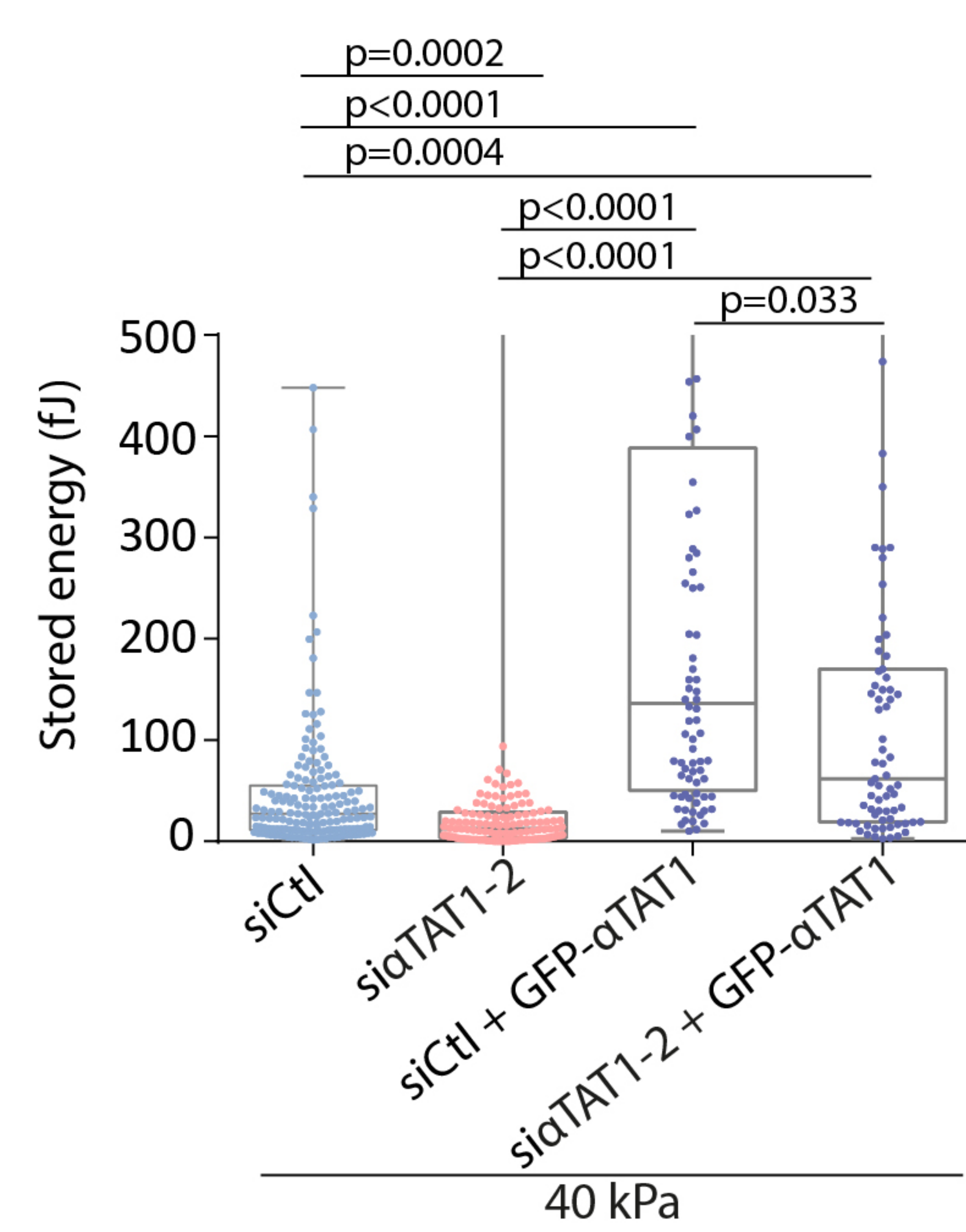
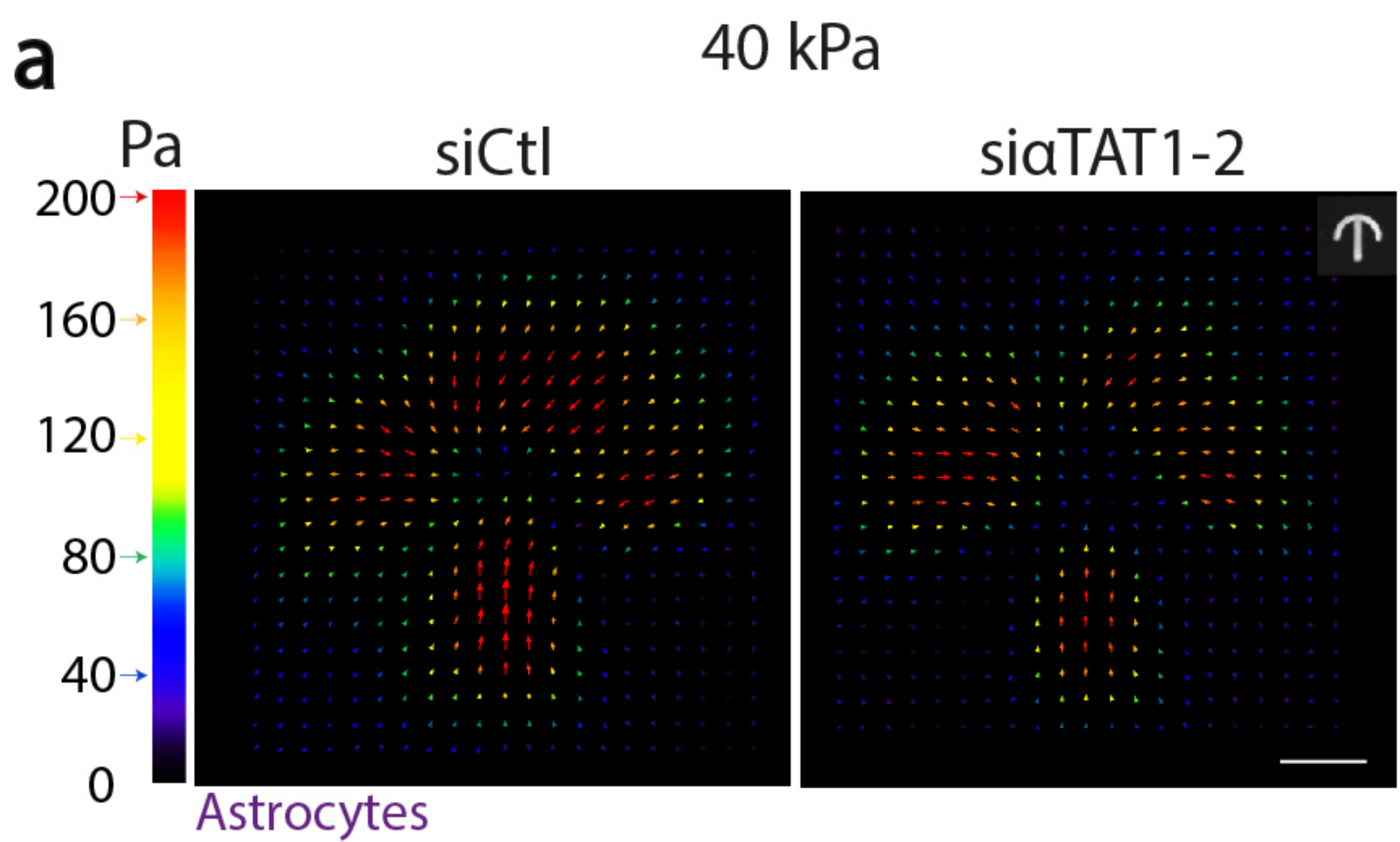
985

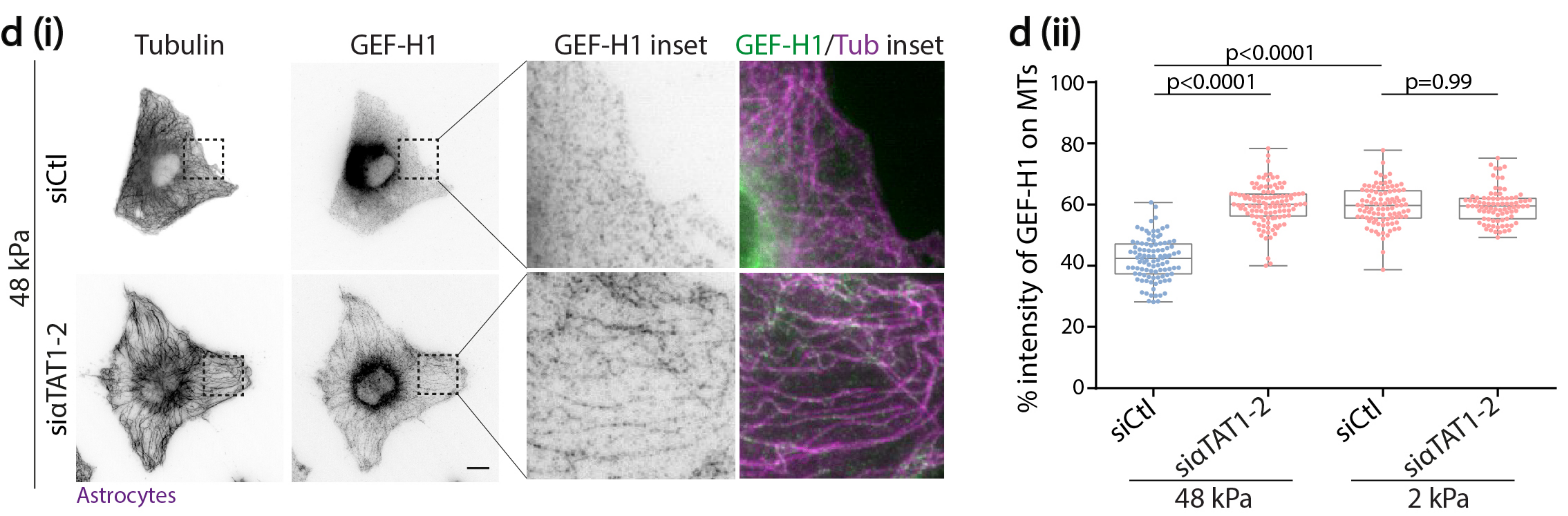
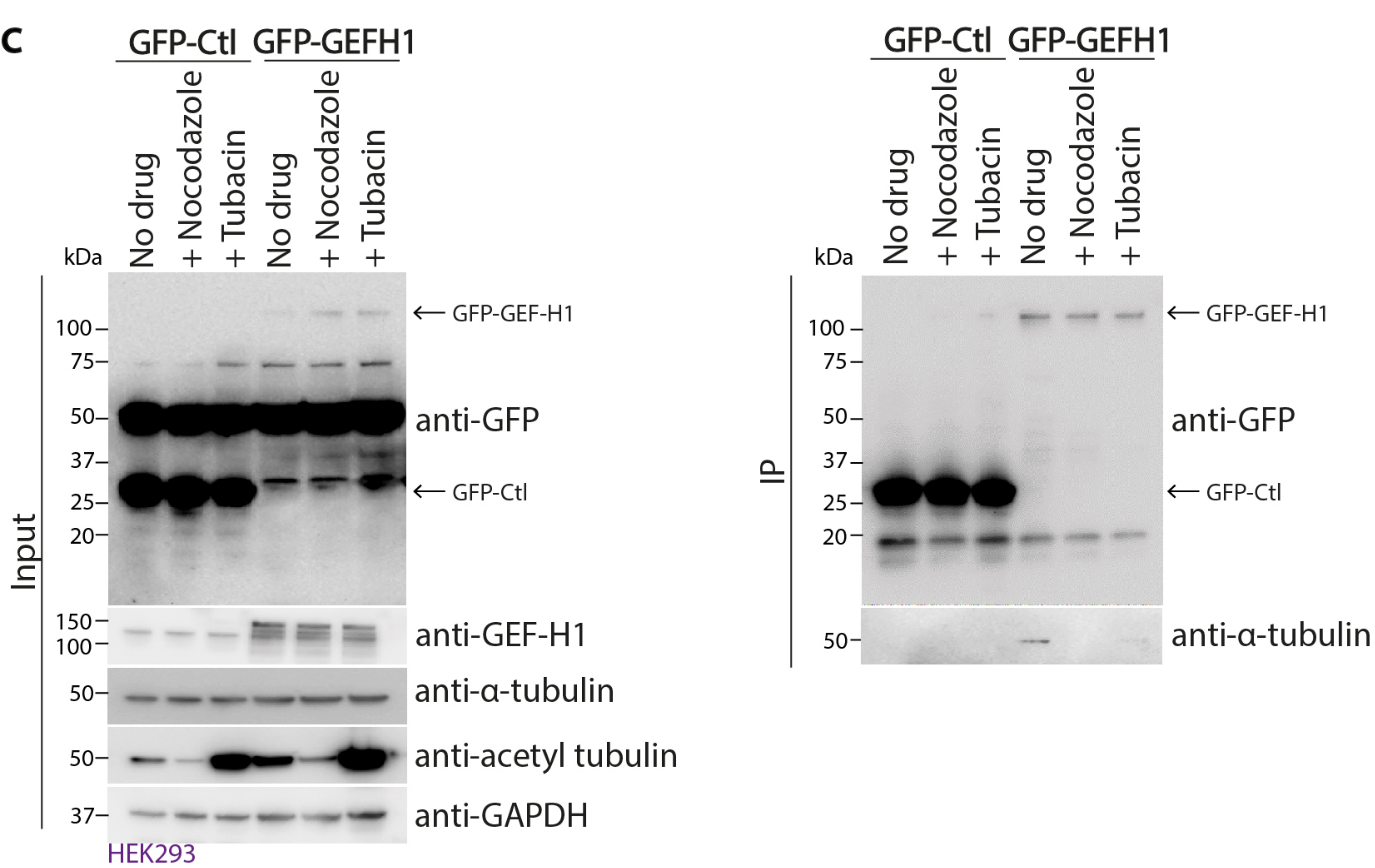
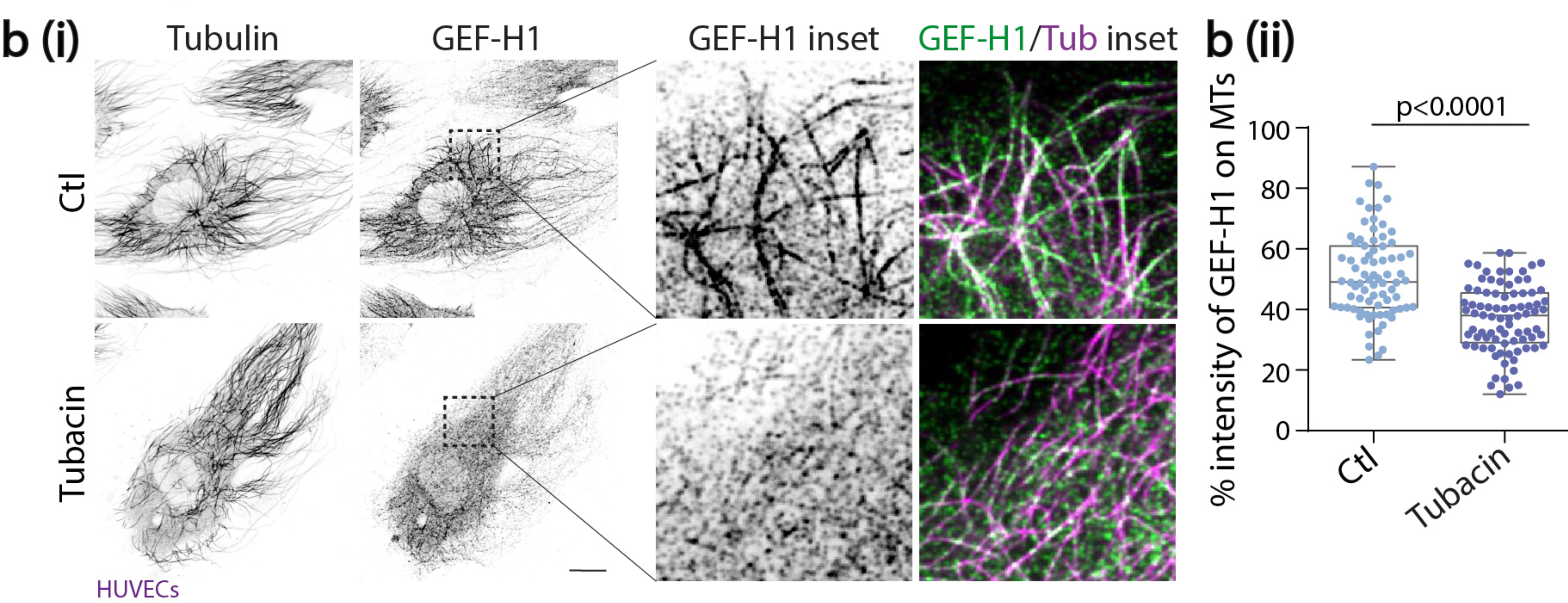
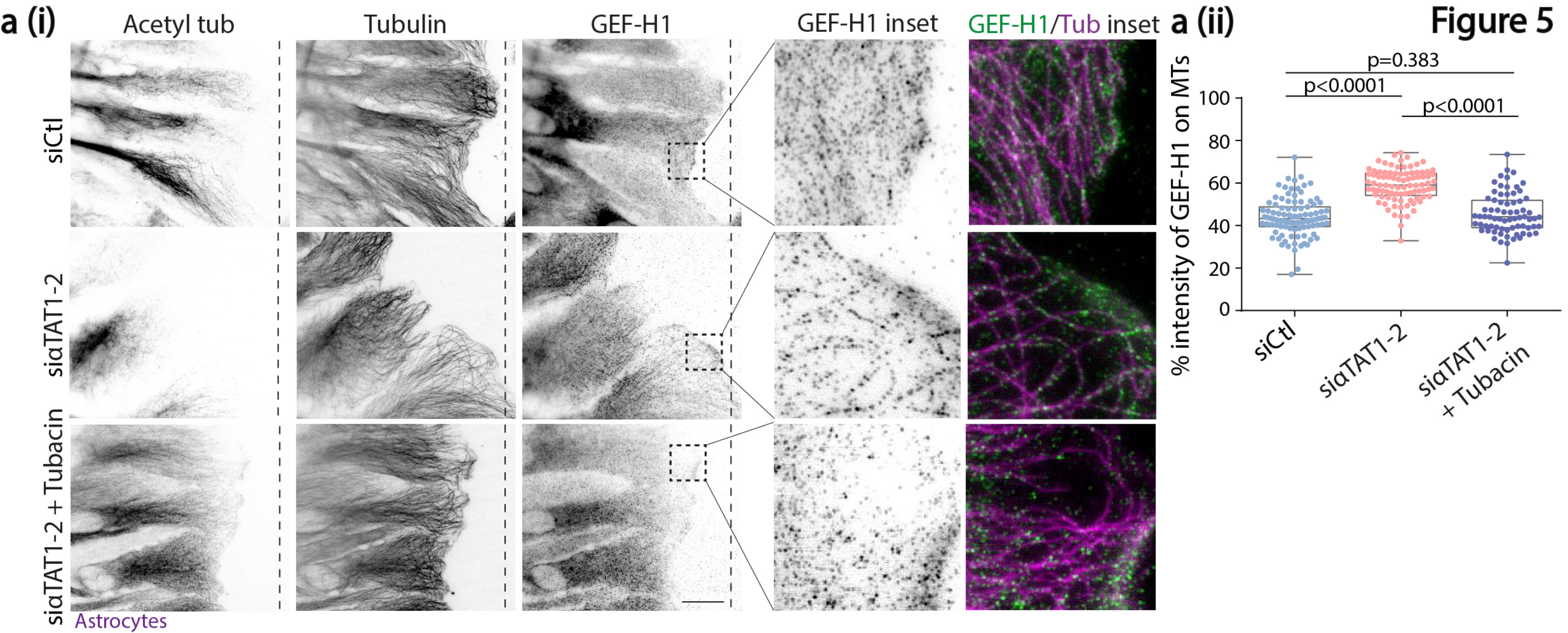
986

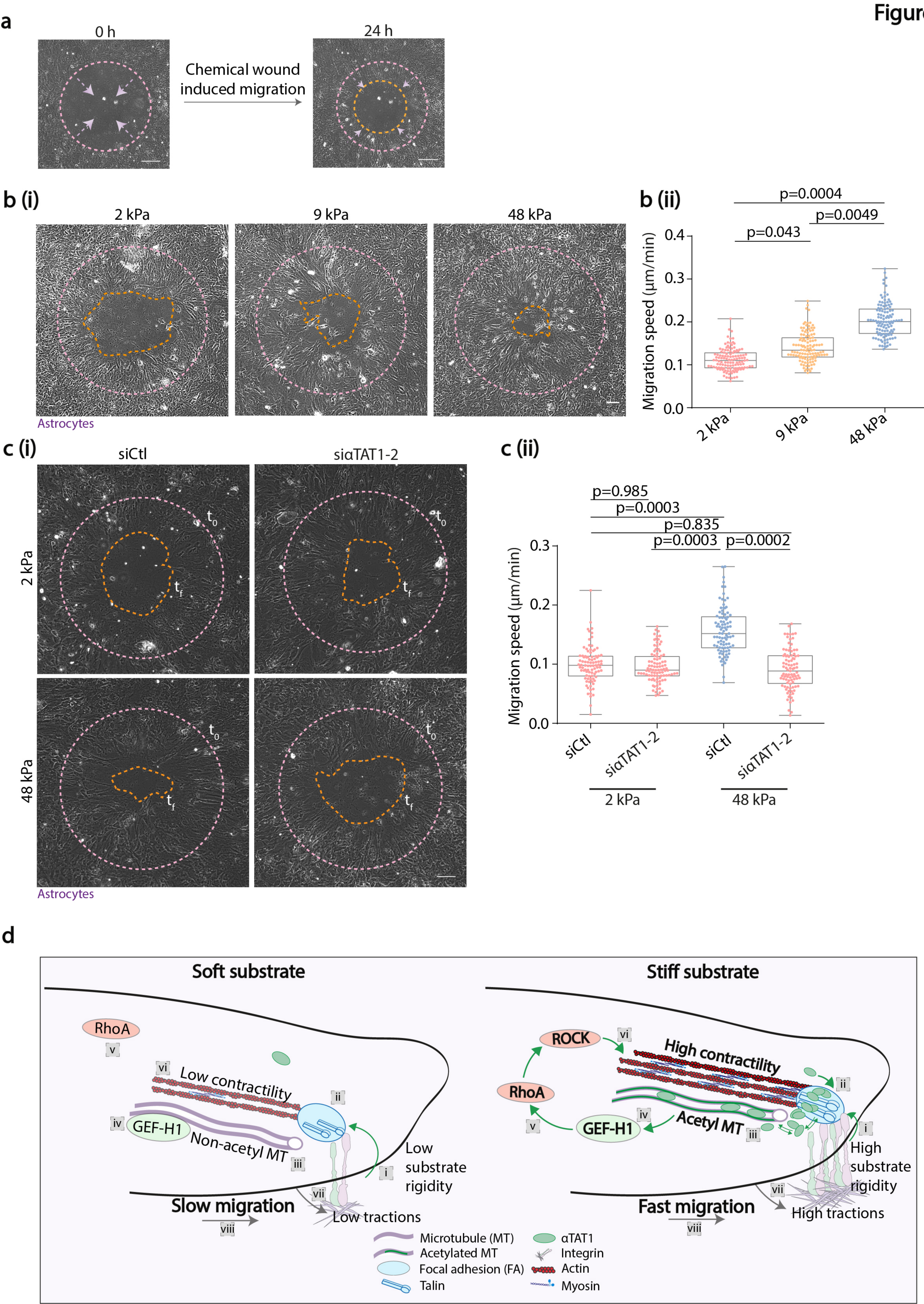




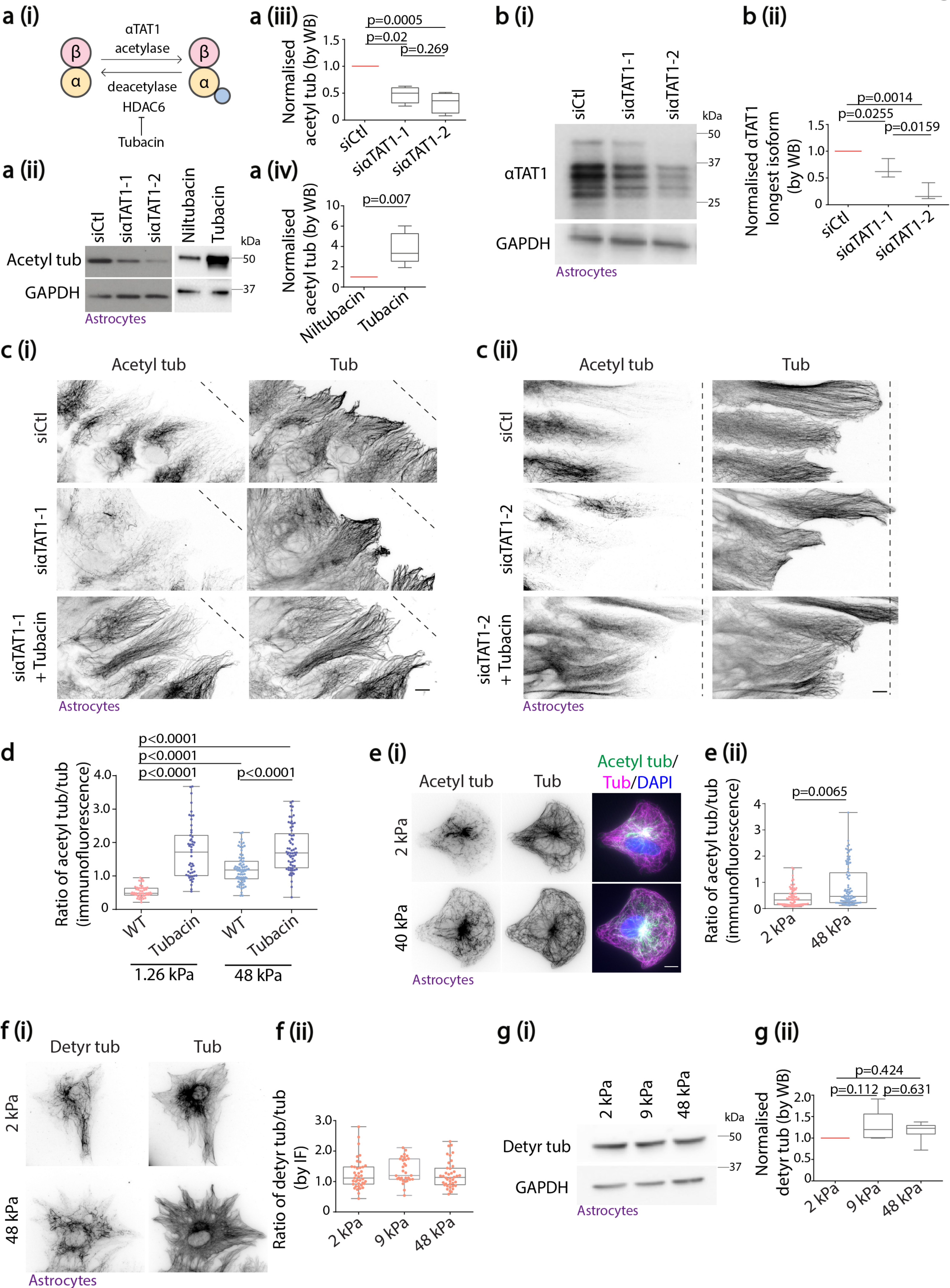


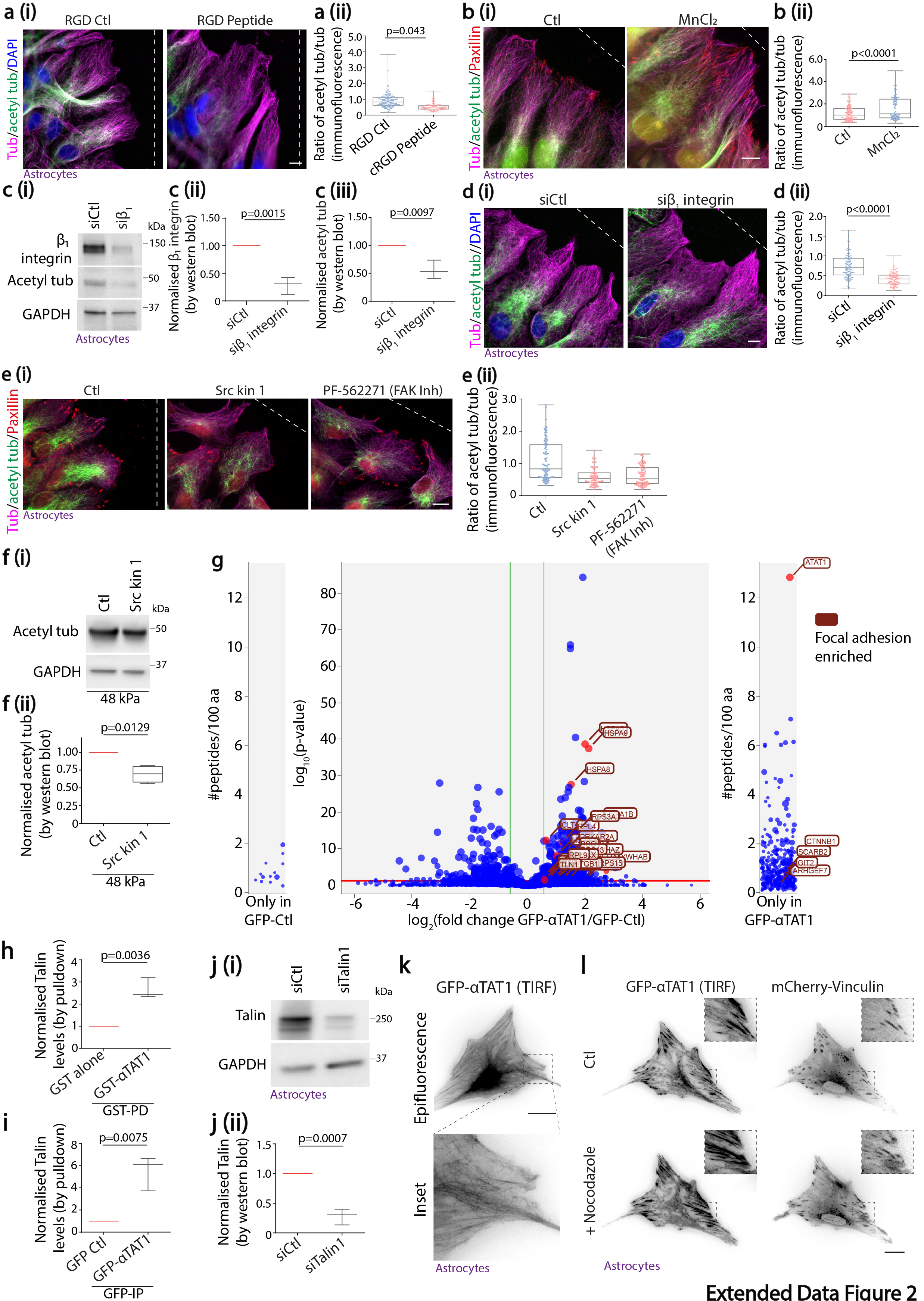




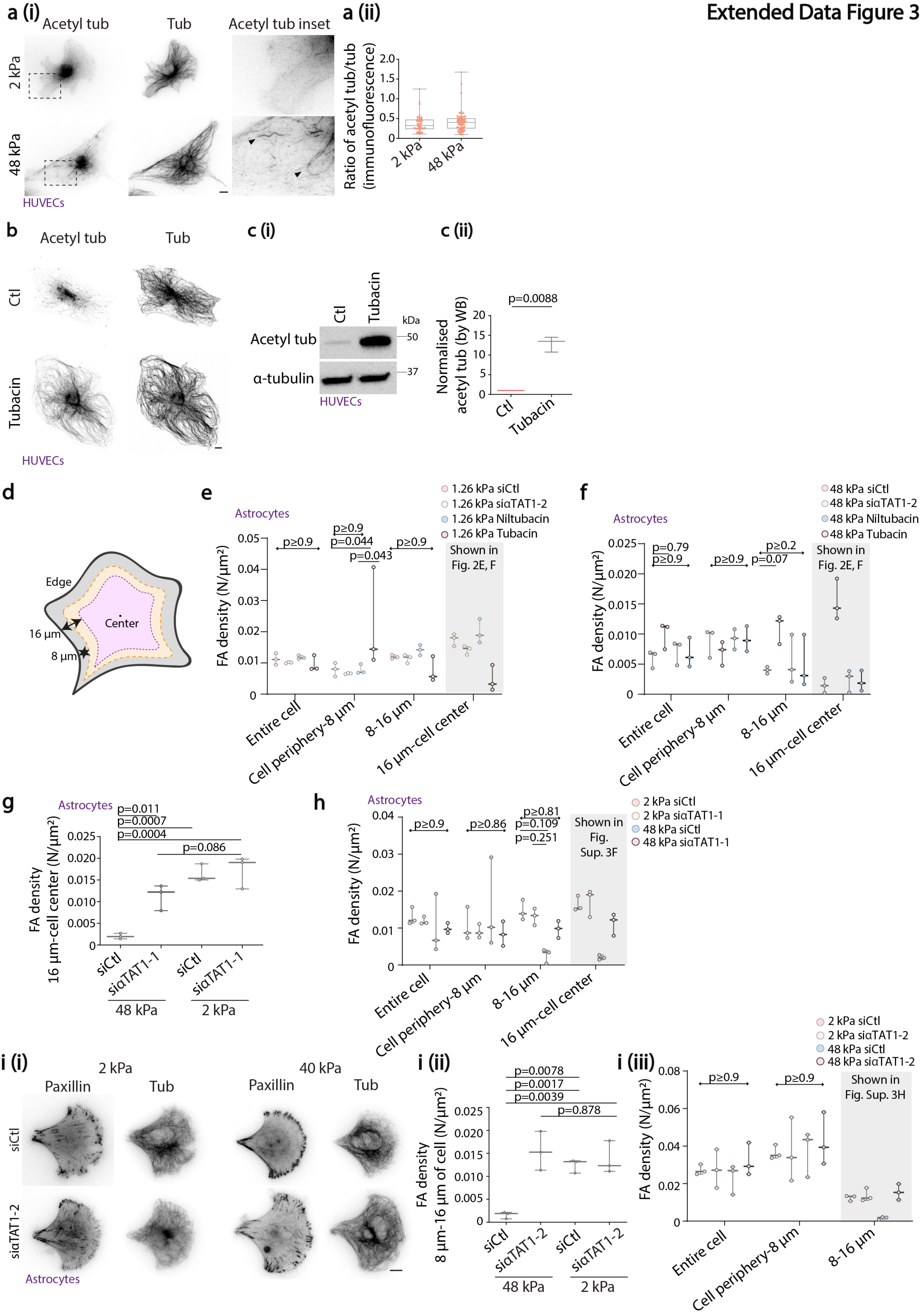




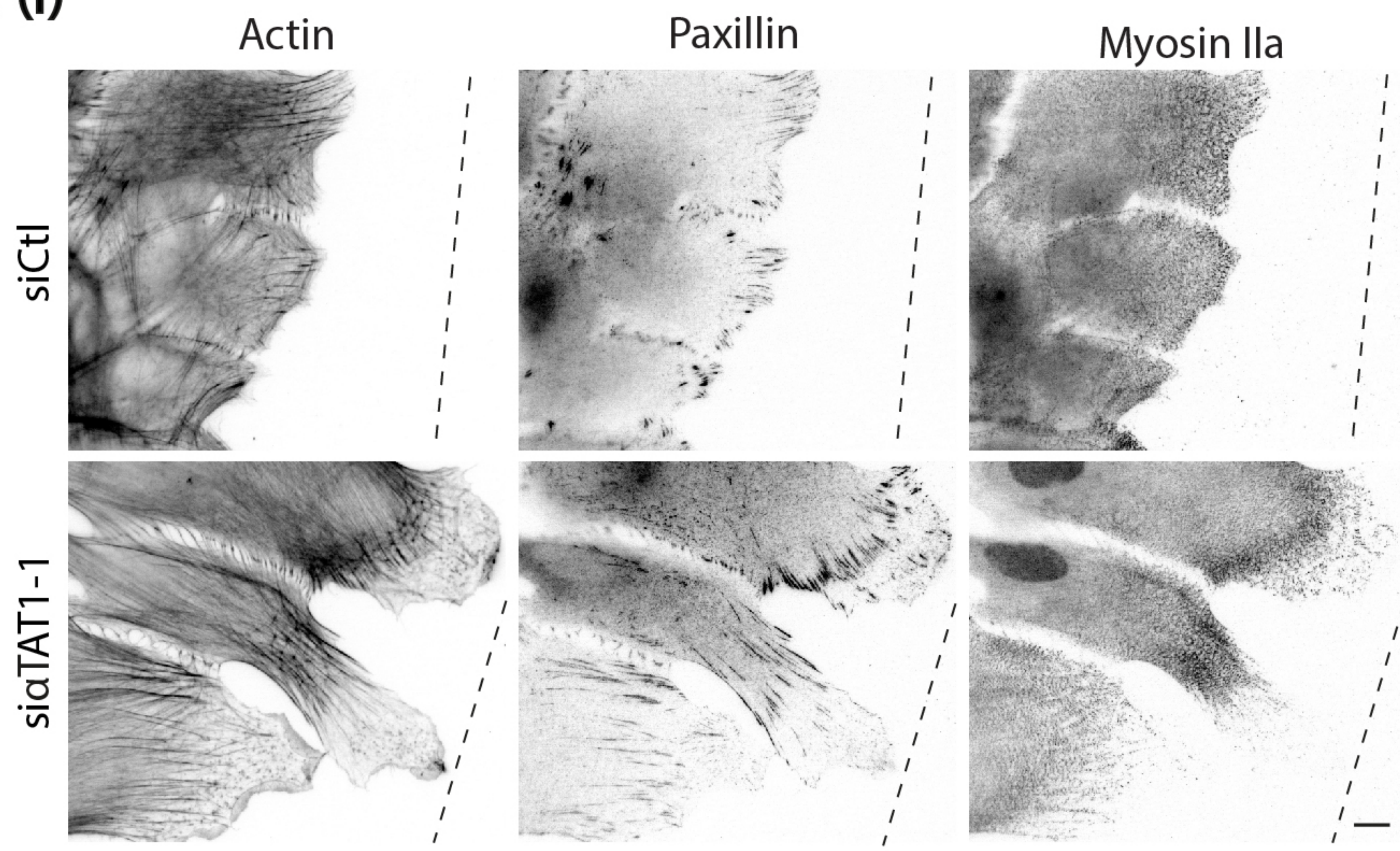




Extended Data Figure 2



**a (i)**



**a (ii)**

